VORTEX RING STATE PREDICTION AND ANALYSIS

Paul Mullen
Leonardo Helicopters, Yeovil, UK

Gianni Bernini
Leonardo Helicopters, Yeovil, UK

1 ABSTRACT

The Vortex Ring State (VRS) phenomenon is a hazardous aerodynamic condition that requires study and understanding. VRS may occur under descending flight conditions with relatively high velocity or at steep descending flight path angles. This paper will look into the VRS phenomena through simulation. This will involve discussion of VRS calculations starting with basic momentum theory before moving through to extended momentum theory. From this theoretical approach a Matlab® routine that defines a rotorcrafts VRS envelope for an isolated rotor will be discussed. The final part of the paper discusses the results of attempting to model the VRS condition in CFD using the HMB and FLUENT programs.

2 ACRONYMS AND DEFINITIONS

AW	AgustaWestland
CFD	Computational Fluid Dynamics
HMB	Helicopter Multi-Block
VRS	Vortex Ring State
VTOL	Vertical Takeoff and Landing
NACA	National Advisory Committee for Aeronautics
V_x	Forward Velocity
V_z	Descent Velocity
vh	Hover Induced Velocity
μ	Rotor Horizontal Velocity normalised by Hover Induced Velocity
η	Rotor Vertical Velocity (+ve in climb) normalised by Hover Induced Velocity
v	Induced Velocity normalised by Hover Induced Velocity
κi	Induced Power Factor
k	Empirical Inflow Factor
ε	Empirical Factor, Vortical Structures Critical Velocity
C_T	Thrust Coefficient
NATOPS	Naval Air Training and Operating Procedures Standardisation

3 INTRODUCTION TO VRS

A helicopter rotor in real flight generates a downward flow (downwash) induced by the thrust generation. If the rotor is moving downward, along the direction of its induced flow, the downwash mixes with the upward flow due to the descent motion. The rotor flow near the rotor disk is dominated by the rotor-induced velocity while the surrounding flow moves upwards. For VRS to occur, the up flow must be of the same order of magnitude as the rotor-induced velocity. In VRS, the wake vorticity cannot sweep away from the rotor. Instead, it accumulates near the rotor plane until a violent and unsteady flow condition takes place with the formation of a doughnut-shaped ring of re-circulating airflow. Entry into the VRS manifests through different effects such as strong thrust fluctuations, torque oscillations, increased vibration levels and loss of control effectiveness. One of the biggest effects is a significant increase in the descent rate for a helicopter or a roll-off for a tiltrotor. Flow visualisation of VRS can be seen in figure 1.

An increase in the average power required to overcome higher aerodynamic losses can also occur. Most helicopters do not have any excess power available at low airspeeds. Therefore, when in VRS, the application of high rotor torque may be sufficient just to maintain equilibrium flight, even though the aircraft is rapidly descending. This phenomenon is often referred to as "settling with power" or "power settling" and comes from the fact that the helicopter keeps settling even though full engine power is applied. Some situations that are conducive to a settling with power condition are:

1. Any hover OGE (out of ground effect) above the hovering ceiling of the helicopter
2. Downwind and steep power approaches with little forward airspeed. Vertical descent of at least 300-500 ft/min, depending on disk loading, gross weight, rpm, density altitude and powered flight using 20-100 percent of the engine power
3. Quick-stop type manoeuvres
4. Recovery/entry into autorotation
5. When descending downwind into a landing area

Washizu et al. have tried to quantify the effect of VRS on the increase in terms of induced power required through an induced power loss factor:

$$\kappa i = \frac{P_i}{T v_i} \quad (1)$$

where Pi is the measured/estimated induced power during equilibrium descent through VRS, T

is the thrust and v_i is the rotor mean induced velocity as given by the simple momentum theory. The measured data showed the variation of κ with descent velocity and collective [1].

4 LITERATURE OVERVIEW

A number of wind-tunnel experiments and flight tests have been performed over the years. A summary of the experiments on VRS utilised in this work are presented in table 1. The full scale flight tests are considered for validation purposes in this paper.

4.1 Castles and Gray (1951)

Castles and Gray performed wind tunnel tests to derive an empirical relation between the induced velocity, thrust and rate of vertical descent of a helicopter on four model rotors. The model tests covered the useful range of C_T and the range of vertical descent from hovering to descent velocities slightly greater than those for autorotation. The blade models, each of which had an effective solidity of 0.05 and NACA 0015 blade aerofoil, had various chord and twist parameters. The correction for blade dynamic twist has been incorporated into the final data and the following general observations have been made from these tests:

I. The wind-tunnel tests showed no significant variation in the inflow curves due to different thrust coefficient, rotor speed and rotor diameter.
II. The main effect of twist was to increase the ideal rate of descent of autorotation by 10 percent. Also the peak value of the non-dimensional induced velocity was increased by approximately 24% over that for the rotor with untwisted blades and the peak occurred at a rate of descent that was 17% higher.
III. Thrust and torque fluctuations on the rotor with twisted blades were much larger at higher rates of power-on descent than those for the rotors with tapered or untwisted blades.

4.2 Taghizad (2002)

Taghizad et al. conducted experimental and theoretical investigations of a helicopter operating in VRS. The aircraft was an Aérospatiale SA365 Dauphin 6075 tested at the French Flight Test Centre (CEV). The mean induced velocity has been estimated from power measurements in flight. The test has been carried out by following two different flight procedures to enter vortex ring state: from level flight at a given forward velocity, the collective was progressively decreased until the helicopter entered in VRS; or from descending flight, the forward speed was gradually decreased until VRS was reached. In that way, the upper and lateral VRS boundaries have been derived. During the tests, the main VRS characteristics were a sudden drop in vertical speed Vz (from -5 m/s to -15 m/s) and an increased level of vibrations with the helicopter being very unstable and hard to control during the fall. The rate of descent was found to be insensitive to collective, however VRS effects disappeared with a forward velocity Vx/Vh = 1. Taghizad et al. also concluded that VRS was difficult to predict because of its intrinsic turbulent and chaotic nature. Two VRS flights starting from close conditions could result in very different helicopter behaviours.

4.3 V-22 IIT FLIGHT TEST PROGRAM (2003)

In August 2003, extensive flight tests were conducted in order to investigate V-22's low speed VRS characteristics. Tests probed deeply into fully developed VRS to determine a vortex ring state flight envelope and to demonstrate the ability of the V-22 to recover. The V-22 testing has shown that the aircraft in fully developed VRS exhibits lateral control asymmetry followed by non-commanded roll response and strong thrust fluctuations. It was also found that the VRS boundaries between the tiltrotor and the conventional helicopters was remarkably similar. High blade twist and the side-by-side rotor configuration of the V-22 did not play a significant role in defining the VRS boundaries. However, high disk loading allowed higher rates of descent before VRS symptoms were encountered and also extended the VRS boundary towards higher forward airspeeds.

5 WORKING STATES OF THE ROTOR IN AXIAL FLIGHT

This section deals with the problem of defining a rotor inflow model valid throughout the typical operating range of a rotor. Before entering into details, it is worth giving a quick review of the four rotor operating conditions in vertical flight. Defining with V_z the axial vertical speed of the helicopter, with V_h the induced velocity in hover and with V_{tr} the transition velocity between VRS and the turbulent wake state region, it is possible to define the following phases:

1. Normal working state, $\frac{Vz}{Vh} \geq 0$: The normal working state region includes climb and hover. Tip vortices follow a smooth, helicoidal-like trajectories and the slipstream is always well defined. The flow is highly periodic and free from any significant disturbances. Momentum theory is therefore valid, resulting in good estimates of rotor performance.

2. Vortex Ring State, $\frac{\mathrm{Vtr}}{\mathrm{Vh}} \leq \frac{\mathrm{Vz}}{\mathrm{Vh}} \leq 0$: In VRS a defined slipstream does not exists anymore. The flow becomes highly turbulent and unsteady with the tip vortices being convected very close to the rotor plane. The wake accumulates and large recirculation occurs, resulting in rotor vibrations, degraded control, significant blade flapping and increase in sink rate. In this region momentum theory is invalid.
3. Turbulent Wake State, $-2 \leq \frac{\mathrm{Vz}}{\mathrm{Vh}} < \frac{\mathrm{Vtr}}{\mathrm{Vh}}$: As the descending velocity increases further, flow recirculation through the rotor diminishes as well as rotor vibrations. However the rotor still experiences some roughness due to the high turbulence and aperiodicity of the flow in this condition. It is also the region in which equilibrium autorotation occurs. This state represents the initial return to a smooth flow with a well-defined slipstream boundary and the flow is similar to that associated with a bluff body. Momentum theory is still invalid.
4. Windmill Brake State, $\frac{Vz}{Vh} < -2$: This condition occurs at high descent rates with the flow being again smooth with a well defined upwards slipstream. The condition takes its name from the fact that the rotor is extracting energy from the flow and brakes the flow velocity like a windmill. Momentum theory is applicable, providing good rotor performance estimates.

6 MOMENTUM THEORY FOR INDUCED VELOCITY PREDICTIONS

The flow state around a helicopter rotor is a global phenomenon that involves several parameters which can be found in [2] and [3]. From dimensional analysis it follows that the appropriate scale velocity of the flow is defined by:

(2) $$v_h = \sqrt{\frac{T}{2\rho A}}$$

where v_h is the rotor ideal induced velocity in hover, T is the thrust, ρ is the density and A is the rotor disk area. The flow state depends on vertical velocity V_z and horizontal velocity, V_x, or, alternatively, on the rotor angle of attack α. Momentum theory can provide an estimate of the rotor induced velocity only in certain conditions and under specific limitations. Momentum theory refers to the conservation of mass, momentum and energy in case of an inviscid, incompressible, steady and non-rotational flow. The rotor is modelled as a circular disk that sustains a pressure jump (actuator disk). It is assumed that a well-defined slipstream boundary exists and the rotor power can be derived for a given thrust. Uniform induced velocity and uniform pressure at the rotor disk are assumed. The basic general momentum theory equation for a rotor is provided as follows:

(3) $$\nu\sqrt{\mu^2 + (\nu + \eta)^2} = 1$$

where ν, η, μ represent normalised values of induced velocity, horizontal speed and vertical speed respectively. Equation 3 is essentially a steady state first order representation of the average induced velocity across the rotor. The normalisation is carried out by means of the ideal induced velocity in hover so that:

(4) $$\nu = \frac{V_i}{v_h}, \qquad \eta = \frac{V_z}{v_h}, \qquad \mu = \frac{V_x}{v_h}$$

In axial descent, μ = 0 and the previous equation can be further simplified as:

(5) $$\nu^2(\nu + \eta)^2 = 1$$

For pure axial flight (Vx = 0), momentum theory provides the following solution for the induced velocity:

(6) $$V_i = -\frac{Vz}{2} + \sqrt{\left(\frac{Vz}{2}\right)^2 + {V_h}^2} \qquad for\ Vz > 0$$

(7) $$V_i = -\frac{Vz}{2} - \sqrt{\left(\frac{Vz}{2}\right)^2 - {V_h}^2} \qquad for\ Vz < -2V_h$$

(8) $$V_i = -\frac{Vz}{2} + \sqrt{\left(\frac{Vz}{2}\right)^2 - {V_h}^2} \qquad for\ Vz < -2V_h$$

The power required in axial climbing and descending flight is a function of the axial speed and induced velocity. The non dimensional power ratio can be expressed as:

(9) $$\frac{P}{P_h} = \frac{V_z + V_i}{V_h} = \frac{V_z}{V_h} + \frac{V_i}{V_h}$$

The two terms on the right hand side of the previous equation represent the work done to change the potential energy of the rotor and the work done on the air by the rotor respectively. Following, the power ratio for climb is:

(10) $$\frac{P}{P_h} = \frac{V_z}{2V_h} + \sqrt{\left(\frac{V_z}{2V_h}\right)^2 + 1} \qquad valid\ for\ \frac{V_z}{V_h} \geq 0$$

In descent, the power ration is given by:

(11) $\frac{P}{P_h} = \frac{V_z}{2V_h} - \sqrt{\left(\frac{V_z}{2V_h}\right)^2 - 1} \quad valid\ for\ \frac{V_z}{V_h} \leq -2$

6.1 Momentum Theory Limitations and Singularity

In the region -2 ≤ Vz/Vh ≤ 0 it is not possible to calculate the rotor inflow directly because momentum theory is not valid. The flow can take on two possible directions and a definite slipstream does not exists anymore. Descending flight in deep VRS accentuates the interactions between the tip vortices and the other blades so the flow becomes rather unsteady and turbulent and experimental measurements of rotor thrust and power are difficult to make.

The induced velocity solutions are plotted in figure 2 where it is possible to see three branches. The upper branch (in blue), corresponding to equation 6, is often called the helicopter branch while the lower branch (in green) corresponding to equation 7 is the windmill branch. Both the helicopter and the windmill branches are valid solutions. However, the branch corresponding to equation 8, in red, is not valid because it violates the assumed flow model and represents a non-physical solution. Considering the gap between the stable branches and the fact that momentum theory is invalid in the range -2 < Vz/Vh < 0 it appears evident the difficulty to derive an induced velocity curve. However, the induced velocity distribution can still be defined empirically on the bases of flight tests or wind tunnel experiments. The experimental campaign selected to build the semi-empirical model presented in this report is the Castle and Gray [4].

Figure 3 presents the inflow data obtained by Castles and Gray and the results obtained from momentum theory. The experiments describe the influence of twist as an increase in rate of descent at ideal autorotation by 10%; peak V_i/V_h increased by 24% at 17% higher V_z/V_h; moreover, measured fluctuations in force and moment were much larger.

By comparing the theoretical results with the wind tunnel data, three aspects are noteworthy. First, the momentum theory under-predicts the values of induced velocity along the helicopter and the windmill branches. The increment of induced velocity is clearly non-linear with a peak of induced velocity at V_z/V_h = -1.5. Second, the experimental data shows a transition between the blue (helicopter) and the green (windmill) branches while no transition is predicted by momentum theory. Third, the experimental data exhibits considerable scatter due to strong fluctuations caused by the rotor operating in VRS regime.

One of the main reasons why momentum theory under-predicts the induced velocity is related to the interaction between the rotor wake and the surrounding airflow which is not taken into account by the actuator disk theory. The momentum theory ignores all the non-ideal induced losses, including effects of a finite number of blades and non uniform loading. For all those aspects, test data must be the basis for the induced velocity in vortex ring state and turbulent wake state, where momentum theory in not valid. The empirical relation between induced velocity, thrust and rate of vertical descent of a helicopter was calculated indirectly by Castles and Gray from the measured rotor power and thrust. The measured rotor power can be written in the form:

(12) $\boldsymbol{P = T(V_Z + v) + P_0}$

where P is the measured rotor power, T is the thrust, V_z is the vertical axial speed, v is the mean induced velocity and P_0 is the rotor profile power. Therefore, to obtain an estimate of v, in addition to P_0, T and V_z is necessary to know the rotor profile power. A method to get an estimate of the profile power is to perform an element-by-element analysis of sectional drag forces and to integrate radially along the blade span:

(13) $\boldsymbol{P_0 = \Omega N_b \int_0^R D y d_y}$

where N_b is the number of blades, Ω is rotational speed and D is the drag force per unit span at a distance y from the rotational axis. If the section profile drag is assumed to be constant and independent from Re and Mach and the blade is not tapered in planform (i.e. rectangular), the profile power can be written as:

(14) $\boldsymbol{P_0 = \frac{1}{8}\rho N_b \Omega^3 c C_{d0} R^4}$

with ρ being the density, c the section chord, C_{d0} the constant section profile drag coefficient and R the rotor radius. At this point the induced velocity can be calculated by using:

(15) $\mathbf{v = \frac{P - P_0}{T} - V_Z}$

6.2 Extended Momentum Theory

The first step in order to obtain a complete and realistic induced velocity curve based on experimental results is to eliminate the singularity of momentum theory and remove the unstable

branch from the curve reported in Figure 2. The result of this step is referred to as the baseline model. The next step is to bridge the gap between the two stable branches and build the region of negative slope in vortex ring state. To solve this problem, two convenient points of the V_z/V_h range have been chosen in function of the forward speed V_x/V_h and a cubic spline interpolation was used in Matlab® to model the transition in VRS. This approach is designed to eliminate the singularity of the momentum theory in axial descent flight and to obtain a preliminary inflow model known as extended momentum theory, which extends its validity in the region where momentum theory does not provide meaningful results.

6.3 Corrected Momentum Theory

The 'extended momentum theory' model, however, under-predicts the induced velocity because of the ignorance of the interaction between the rotor wake and the surrounding airflow. So far, the model is based on a pure theoretical analysis, neglecting the flow recirculation near the rotor disk as well as all the additional non-ideal losses. As a helicopter increases its descent rate, the flow interaction between the up flow outside and the downwash inside the rotor wake becomes stronger and stronger, eventually with the formation of a series of vortex rings located at the rotor periphery. Some comparison have been made with the Castle and Gray experiments [4].

Figure 4 suggests that the extended momentum theory needs to be corrected. The extended model requires an increment (with respect to the extended model), ΔV_{VRS}, that takes into account for the normal velocity of the vortices that accumulate on the rotor plane. The velocity increase is defined by the maximum inflow value predicted by the extended model V_{PEAK} at η_{PEAK} and the inflow values in hover, V_h at $\eta = 0$. This increment is then multiplied by a damping function f, based on the inflow characteristics, which allows the instability in VRS to be reduced (if $f \neq 0$) or suppressed (if $f = 0$). An induced power correction factor, κi is also introduced to account for the non-ideal, but physics effects, such as non-uniform flow, tip losses, finite number of blades and so on, that characterise uniquely a specific rotor. Values of κi can be computed from rotor measurements, flight tests, CFD simulations and other advanced blade element methods with a typical average value being 1.15. The induced power factor is linked to the figure of merit as follows:

$$\textbf{(16)} \qquad FM = \frac{P_{ideal}}{P_{real}} = \frac{P_{ideal}}{\kappa i * P_{ideal} + P_0} = \frac{1}{\kappa i + \frac{P_0}{P_{ideal}}}$$

The final inflow corrected value is [5]:

$$\textbf{(17)} \qquad v = \kappa i \, (v_{base} + f \Delta V_{VRS})$$

Figure 5 shows three different inflows corresponding to three different induced power factors of 1 (ideal), 1.1 and 1.2 for a pure axial descent flight ($\mu = 0$). The comparison between the corrected model, the baseline extended model and the experimental results from Castles and Gray is presented in figure 6.

The good correlation between measured and calculated rotor induced velocity confirms that the inflow model is fairly accurate considering the difficulties involved in obtaining such inflow information in VRS. Outside VRS, like in climb or fast descent, the effect of the term ΔV_{VRS} diminishes because the tip vortices are swept away from the rotor plane. Based on the available measured data, a comparison is hereafter presented between the semi-empirical induced velocity model form corrected momentum theory and experimental results. Figures 7 and 8 use the Castle and Gray wind tunnel data for comparison whilst figure 9 the Taghizad flight test data. For all plots a continuous black line represents the inflow predicted by the corrected momentum theory.

7 VORTEX RING STATE MODEL

In order to derive a vortex ring state boundary, it will be necessary to couple the inflow model with a VRS criterion. The selected criterion has to be capable of considering the balance between the rate of growth of tip vortices and the rate (speed) at which these structures are swept away from the rotor. The most widely utilised vortex ring state prediction algorithm is that of Dr. J. Wolkovitch. There are a couple of deficiencies with the Wolkovitch model that mean the VRS boundary predictions from it are not sufficiently accurate to be used as a warning algorithm. These are:

1. The inflow model considers only a downward vertical velocity for the vortex cores. There are no horizontal or in-plane velocity components for the rotor's wake. This is not supported by available test data and doesn't make sense considering that, according to this model, VRS is possible for all horizontal velocities.
2. The lower boundary predicted by Wolkovitch does not separate correctly from the vortex ring state regime into the windmill brake state. H-34 flight tests show data points that lie below the lower boundary described by Wolkovitch's model.

A model developed by Taghizad et al. is based on the mean convection of tip vortices and takes into account for both vertical and horizontal components of the tip vortices. The VRS criterion is presented below in its non dimensional forms:

$$\sqrt{\left(\frac{\mu}{k}\right)^2 + \left(\eta + \frac{\nu}{2}\right)^2} \leq \varepsilon \quad \textbf{(18)}$$

$\mu=V_x/V_h$ is the non-dimensional horizontal speed, $\eta=V_z/V_h$ the non-dimensional vertical speed, $v=v_i/V_h$ the non-dimensional induced velocity, k is a factor that accounts for the tendency of the tip vortices to stay in the plane of the disk and ε dimensionally equivalent to a velocity and represents the VRS critical velocity.

According to equation 18, an isolated rotor is supposed to enter in vortex ring state when the combination of horizontal velocity V_x, Vertical velocity V_z and induced velocity v equals the critical VRS velocity ε. In this case, the net velocity through the rotor is insufficient to sweep away vorticity from the rotor plane causing the air to be pushed downward through the rotor, then radially outwards and upward above the rotor, circulating in a manner from which this state derives its name. The values of the parameters k and ε have been taken in line with the values suggested by Taghizad et al. because they provide good results in comparison with the flight tests. The numerical values have been chosen to be:

k = 4
ε = 0.2

A Matlab® routine and an Excel® based spreadsheet have been implemented in order to derive the VRS envelope starting from the basic momentum theory applied to the isolated rotor. The routine scheme is presented in figure 10.

The Matlab® script is structured into three main sections. The first part of the code is dedicated to the inflow model. The basic momentum theory equation is solved for a wide range of vertical and horizontal velocities. Then the script deals with the interpolation of the basic inflow curves to get the extended version of the momentum theory. At this stage the singularity at μ = 0 is removed and the transition between the helicopter branch and the windmill branch is smoothed. The last part of the first section is where the correction algorithm based on the experiments of Castles and Grays kicks in, providing the final solution for the inflow.

The second part of the code is dedicated to the VRS criterion based on the previously mentioned Taghizad model. The script uses equation 18 to get the combinations of μ, v and η that give the VRS boundary for the specific isolated rotor. The input required are:

I. Rotor radius
II. Aircraft weight
III. Air density
IV. ki factor to account for additional induced losses (specific for the rotor)

The third and last part of the code is dedicated to plotting. A complete VRS envelope is presented in three different ways: in [m/s], in [ft/min] against [knots] and in a non-dimensional format. The rotor inflow is plotted as well.

7.1 Analytical Prediction of the Vortex Ring State Boundary

The result of the Matlab® routine is presented hereafter. The test case has been selected to be the Bell XV-15 tiltrotor, the first successful experimental tiltrotor to demonstrate high speed performance relative to conventional helicopters. The script was run for different aircraft weights and flying altitudes (table 2) to highlight the impact of those parameters on the VRS envelope. Figure 11 shows how a change in these attributes can affect the location and size of the boundary.

The rotor radius is 3.81m and the additional hover induced losses factor k has been set to 1.1 for the first 6 cases. However, the effect of k factor required analysing. As such two cases with different k factor values are shown in table 3. Figure 12 shows the effect this has on the VRS boundary.

7.2 VRS Flight Tests and Comparison with the Theoretical Boundaries

This section describes flight experience in the vortex-ring flight condition with the SA365 Dauphin helicopter and the Bell V-22 tiltrotor. An in-depth comparison has been carried out between the flight test data and the analytical model developed in the Matlab® environment, and the validation study was conducted by means of superimposition of the VRS boundaries.

As shown in figure 13, the four bladed SA 365N Dauphin helicopter was tested in 2002 at the French Flight Test Centre [6]. The mean induced velocity of the rotor was calculated from power measurements and the rotor thrust was estimated from the aircraft weight, fuselage drag and rotor's download. Typically, the vertical drag on the fuselage can be up to 5% of the gross weight and the extra rotor thrust to overcome this is:

$$\Delta T = \frac{1}{2}\rho \bar{v}^2 f_v \quad (19)$$

where $\bar{v}$ is the average velocity in the rotor slipstream and f_v is the equivalent drag area. The helicopter was tested in axial flight as well as at forward speeds of 5, 15, 20, 25 and 40 knots. An increased level of vibrations was observed when approaching the VRS regime. Subsequently, VRS manifested as a sudden increase in the rate of descent and the pilot's instinctive reaction to increase the collective did not stop or slow the fall. For the majority of the test, an increase in collective did not strengthen the VRS effects. A part of the test was also performed without the stabilizer resulting in a more stable behaviour in VRS without affecting the VRS entry and exit limits. The helicopter stability boundary from vortex ring state encounter is presented in non-dimensional velocities hereafter and compared with the analytical model. The Matlab script has been set up with the following inputs:

Rotor radius: 5.97 m
Aircraft weight: 3500 kg
Air density: 1.112 (density altitude of 1000 m)
Additional induced losses factor, ki: 1.05

Figure 14 show good correlation between measured and calculated data considering the difficulties involved in predicting a highly unstable and chaotic phenomenon as the vortex ring state. Taghizad et al. also concluded that approaching VRS from two close starting conditions could imply two different helicopter reactions, demonstrating the intrinsic turbulent and unsteady nature of the phenomenon.

In 2003, extensive flight tests were conducted to evaluate VRS effects on the V-22 tiltrotor aircraft [7]. Due to the nature of testing, the manoeuvres have been performed at an altitude ranging from 3000 ft to 9000 ft to allow sufficient altitude to enter and recover. A boom-mounted ultrasonic anemometer was used on the V-22 to provide more accurate velocity readings in the low-speed/high rate of descent regime, as shown in figure 15. Rotor thrust has been measured as a function of the combined yoke beam bending gauges for all blades and both rotors.

During testing, two main parameters have proved to be valid indicators of VRS. The first one is the lateral Automatic Flight Control System (AFCS) that aims at improving the handling qualities of the aircraft and at reducing the pilot's workload throughout the flight envelope. The AFCS helps the Primary Flight Control System (PFCS) with up to 2 inches of equivalent lateral stick input in VTOL mode flight so that the final input = PFCS + AFCS. The lateral stick in tiltrotors controls the differential collective pitch (DCP) and hence the roll motion. When a lateral thrust asymmetry is encountered in VRS, AFCS will automatically apply a lateral control to compensate for the roll disturbance. As VRS builds up, more AFCS authority is required up to the saturation point where the system runs out of authority and the pilot is forced to apply lateral stick through the PFCS to keep the wings level. In further deep VRS, the full lateral stick is not enough to prevent the aircraft to roll-off. The second useful parameter is the Roll Acceleration Error. The final input on the differential collective pitch (DCP) produces differential thrust between the rotor and hence a rolling moment with a subsequent roll acceleration. The roll acceleration error is defined as the difference between the expected roll rate and the actual measured roll rate:

$$\Phi_{error} = \ddot{\varphi}_{exp} - \ddot{\varphi}_{meas} \quad (20)$$

During normal operations, when lateral control is applied the expected roll acceleration is exactly the measured one ($\Phi_{error} = 0$). Since VRS interferes with thrust, roll acceleration error start to increase as the measured acceleration becomes more and more different then the desired one and an un-commanded roll arises. Despite lateral AFCS and roll acceleration error being very useful as VRS indicators, it is worth mentioning an important difference between the two. The lateral AFCS is good in detecting VRS but as soon as it approaches saturation it no longer gives useful information. The roll acceleration error, on the other hand, shows VRS symptoms early on but it is also capable of providing useful information in deep VRS, after the pilot applies full stick.

7.3 Comparison with Theory

Figure 16 and 17 show contours of lateral AFCS and roll acceleration error. The contours are predictors of thrust deficit and uncommand roll. Low level contours mean that the pilot and the AFCS can compensate for the disturbance with sufficient lateral stick input. For high contours value, the full authority of the PFCS and the AFCS will not stop the aircraft from entering in an uncontrolled roll-off unless recovery is initiated. The availability of a clean set of flight test data is of high importance for validation purposes. Calculations were performed for three different C_T values (centred on the average V-22 thrust coefficient during the tests $C_T = 0.016$) and the theoretically derived VRS boundaries have been superimposed to the flight test results shown in figures 16 and 17. Considering the high disk loading and the high blade twist of the V-22, a

factor of 1.08 has been adopted for the additional induced power loss factor in hover.

From figure 18 it is seen that the theoretical limit predicted by the VRS model is in line with the flight tests in terms of forward speed (forward limit). Regarding the rate of descent (VRS upper boundary), the theoretical model shows again an optimistic (by approximately 150 ft/min) prediction compared with the flight tests. Both theoretical and practical results show that the V-22 has a significantly higher rate of descent margin for avoiding VRS with respect to the NATOPS limitation. It must be pointed out that the semi-empirical VRS criterion is somewhat sensitive to the parameters k and ε suggested by Taghizad from the flow visualization of Drees and Hendal. For instance, the sensitivity of the model to the critical effective wake transport velocity ε is shown below for ε = 0.20, 0.21 and 0.22.

Figure 19 shows that better correlation with the experimental data can be obtained by assigning a value of ε = 0.20, as suggested by Taghizad.

Simple engineering analysis show that the V-22's steady state VRS boundary is predictable by simple methods that work for conventional helicopters. Furthermore, the V-22's unique design with high blade twist and side-by-side rotor configuration does not have a significant role in defining the VRS boundary. The most important parameter that affects an aircraft's VRS susceptibility is the disk loading. Consequently, it is fundamental to utilise a representative thrust coefficient in order to predict the VRS limitations correctly.

Dimensional VRS boundaries for different rotorcraft models are presented in figure 20 for ISA sea level conditions. It shows that conventional helicopters are likely to enter in vortex-ring-state regime at lower descent rates compared to tiltrotors. On the other hand, tiltrotors can encounter VRS at higher forward speeds than helicopters. In all situations caution must be exercised to avoid the parameters for settling with power (VRS): 20-100 percent of available power applied and a steep approach. For helicopters and tiltrotors, a normal approach is considered to be a 10 degrees approach. More than 10 degrees is considered to be a steep approach. A steep approach must be used primarily when there are obstacles in the landing path that are too high to allow a normal approach. By examining figure 22 it appears evident that, for a wide range of rotorcraft models, an approach steeper than 30 degrees is considered to be very dangerous and at high risk of VRS.

8 CFD COMPUTATIONS

Due to the unsteady nature of VRS, there has not been many published attempts at simulating a VRS condition in CFD. Within Leonardo Helicopters two CFD codes are used with aerodynamics. These are the University of Glasgow developed HMB [8] and the commercially available ANSYS FLUENT. The following sections discuss the setup and results of the CFD analysis of VRS using the XV-15 aircraft. Initial simulations were computed with ADPanel [9]

8.1 Rotor Geometry

The XV-15 rotor system has three blades with a diameter of 7.62m as stated in table 4. From the available published literature, a baseline XV-15 rotor geometry was created for the HMB and Fluent test cases. The blade chord and twist distributions are published in [10] with the aerofoil identifications and positions found in [11]. As the aerofoil sections were not readily available they were generated using the Ladson and Brooks procedure described in [12]. It is expected that this method provides at least a reasonable approximation of the manufactured shapes. The inboard blade stations have been neglected due partly to the unavailability of the true cuff geometry in the public domain and partly because the panel codes used in the department can only model from 20% radius to the tip. Figure 21 shows the final CATIA® blade.

9 HMB SIMULATIONS

9.1 Input Conditions

For the following HMB work the inputs can be found in table 5. The inputs are all within various stages of VRS with case numbers 2 and 3 being near the centre of the VRS zone.

9.2 Steady Simulations

9.2.1 Setup

Initial simulation inputs were ran with the steady HMB solver. Cases 1-4 were chosen as they represented the region in and around VRS. For these initial simulations the V_x velocity was set at 0 because the steady assumption requires that the flow is axis symmetric. The setup for the simulation was to simulate one third of the model and to set the boundary conditions as periodic. The model boundary and chimera mesh can be seen in figure 22.

9.2.2 Results

Overall the results were mixed as the two cases chosen outside of the VRS zone converged whilst

the two cases inside did not. CFD simulation convergence refers to the residuals in the calculation. Flat residuals are preferred but are only one indicator. Force convergence history of all 4 cases are shown in figure 23. It shows that the thrust coefficient for the slowest descent has the best convergence. The slowest descent also produced the flattest forces with the fast descent producing a sinusoidal pattern. Both of the VRS cases clearly did not converge and do not look likely too even if the simulation was allowed to continue for more iterations.

The results were as expected as using the steady solver assumes that the flow solution the blades pass through is the same for each blade. In a VRS condition the flow is extremely turbulent and separated. The steady solver does not calculate separated flow accurately as it cannot be approximated with periodic assumptions. The Qcrit vortex images below show the flow solution the HMB steady solver had calculated after 50,000 iterations. Figure 24 shows the two cases outside of VRS which show very good stream tubes out by the rotor tips. Figure 25 shows the two cases within VRS which have clearly not resolved the stream tube wake nor the flow at the blade roots.

9.3 Unsteady Simulations

Based on the steady HMB results, an unsteady HMB simulation campaign was launched. The unsteady simulations differ from the steady ones in both the setup and, therefore, the model. Whereas the steady simulations use the periodic boundary condition, unsteady simulations usually do not. This is because the simulation has extremely turbulent and separated flow which means periodic boundaries lead to an incorrect solution. For an unsteady simulation the whole rotor system needs to be modelled, meshed and simulated as one. The mesh, simulation and results are presented in the following sections.

9.3.1 Mesh

The XV-15 rotor model and foreground mesh used in the steady simulations can be used as it is in the unsteady simulations. This is because of the chimera method used in HMB, where multiple meshes can be simulated on together, within certain rules. All of the rotor blades must be simulated in an unsteady simulation as periodic boundary conditions assume the flow is the same coming off of each blade. HMB contains a copy and rotate tool that allows the XV-15 model and mesh to be copied twice and rotated into the correct position at 120° degree steps to generate the full rotor system which can be seen in figure 26.

A new background mesh for unsteady simulations was developed for this project. Usually a mesh is developed to capture the vortex that comes from the tip of the blade and passes under the following blades for a number of turns. As a VRS situation occurs in descending flight, the mesh needs to be developed so it captures the vortex around and slightly above the blades. To do this a new bucket shaped mesh was created and can be seen in figure 27. The rotor system was near the bottom of the mesh which then slowly increased in diameter as it increased in height. The diameter was increased to make sure the vortex was captured even if it started to increase in size or drift away from the rotor tip.

Cell distribution was important. As to how the simulation would develop was unknown, so enough cells were needed to capture the vortex. This had to be balanced out with the amount of time the simulation would require. This is even more important due to the fact unsteady simulations calculate more complex equations so take longer than steady simulations. Therefore an educated guess was taken to determine where best to bunch the cells together to capture the vortex as it interacted with the blades. From the side view in figure 28, it can be seen that the cells were bunched below the rotor system and then slowly increased in size upwards so that any vortex pushed below or above the rotor system was captured. The cells were also bunch from half the blade length to beyond the tip. A side effect to the way the mesh was developed and the amount of cells used, is the large concentration of cells around the root of the blade. This is unavoidable but does mean any root effects are captured. The top down view of the cell distribution shown in figure 29 details how the cells are tightly bunched at the root, expand out over the first half of the blade before contracting over the tip and finally expanding out to the mesh boundary.

The final background mesh is sized at 31million cells, which is three times bigger than a standard steady background mesh. However, a steady background mesh can utilise the period boundary conditions which means only a third of the XV-15 rotor system needs to be generated whilst the full background mesh was required for the unsteady case. With each of the 3 blade meshes required for the unsteady simulations compared to the 1 blade mesh of the steady, the total unsteady mesh is approximately 41million cells. This is nearly three times bigger than the 14million cell mesh used for a XV-15 steady simulation.

9.3.2 Simulation

An unsteady simulation requires a higher number of CPU's than a steady case. For the XV-15 simulations, 400 was an optimum number but 500 were used at some points. For the steady case between 60 and 100 CPU's were used. The VRS case using the unsteady method required 10 turns before the simulation settled down into a VRS pattern. This meant a computational time of around 30 days to complete a full VRS simulation using HMB which is a long time for a modern CFD simulation. However, each turn was 1440 iterations which meant each time step was 0.25° given high accuracy to the simulation. It must be reiterated that the VRS condition is an extremely complex phenomenon with high levels of separated flow being re-circulated back into the rotor system.

9.3.3 Results

Three initial cases were run using the new mesh. These were a VRS case, a fast descent case and a slow climb case. The fast descent and slow climb cases were to be used as validation cases for the new mesh as the results were predicted to be below and above the VRS zone respectively. Full details of the conditions are found in table 6.

The slow climb was used instead of a normal hover case so that the current input files could be used instead of having to set up a hover case and associated files. This case ran very quickly with convergence being reached within 5 full turns as shown in figure 30. The fast descent case took quite a bit longer to converge. This was probably due to the case not being fast enough to have sufficient distance from the bottom of the VRS zone. As figure 31 shows an acceptable convergence was reach but ideally more time could have been spent running this case.

The C_T value calculated for the VRS condition is not unrealistic and is shown in figure 32, which also has the C_Q. It is expected that overall C_T will fall in the VRS region otherwise the rotor would continue to produce enough thrust to keep the aircraft in a stable hover. The forces across the 3 blades began with similar values but soon diverged as the simulation developed. After 10 turns a VRS type condition had appeared. The VRS zone can be seen in figure 33 and shows the how each blade has a varying peak force, yet the mean value of all 3 remains constant. The VRS condition C_T is significantly lower than the slow climb and fast descent cases as shown in figure 34. It does correlate well with the slow climb value but is different from the fast descent. It is possible that due to the close proximity of the VRS zone, the steady and unsteady results were distorted so that they did not correlate. However, the slow climb steady and unsteady correlation gives confidence in the VRS results.

The wake produced by the simulation showed all of the symptoms of VRS. First the rotor produced the trailing vortex that extends back and over the following blade as shown in figure 35. This is expected as the blade pitch and downwards velocity have been calculated to produce this. The flow passing over the blade slowly starts to fall lower so that the blade cuts into it. At this point it is noted that the vortex pulses inwards as it travels part the way along the blade as it cannot dissipate below it. The flow is therefore being re-ingested and the rotor is in a VRS type condition. This continued for a number of turns whilst the flow settled into an oscillating pattern as shown in figure 36. Then the blades began to rise through the vortex. This was unexpected as the flow was expected to continue passing over the blade, as in a real life example the helicopter would have lost lift and fallen through the VRS zone. It can be seen in figure 37. As this is an isolated simulation the downward velocity of the rotors did not increase so the blades were held in state. Eventually the simulation entered into a state where the blades passed in and out of the vortex. The vortex at this time had developed into an oscillating circular cone.

The description of the vortex is backed up by the cut through images of the vortex. They show the development of the vortex and how it is re-ingested after a number of iterations. The turbulence intensity images in figure 38 show how the intensity has increased between 4 and 10 turns. The large red area found in the 10^{th} turn image shows just how turbulent the flow is around the rotor as the values exceed the intended range. The vector images found in figure 39 add to this impression. The vertical velocities found in the 10^{th} turn show the expected flow pattern which give confidence in the validity of the simulation.

10 FLUENT SIMULATIONS

10.1 Input Conditions and Characteristics

For all of the following FLUENT work the inputs (blade collectives and vertical velocities) are the same as the HMB steady simulations. The conditions were chosen based on the theoretical model for VRS boundaries prediction explained in the previous sections with the aim of simulation two cases in deep VRS and two just outside the region to avoid. The selected inputs are found in table 7.

10.2 CFD Model and Case Setup

The computational domain used to simulate the isolated rotor in VRS consists of a bounding box which contains a drum enclosing the rotor and the rotating fluid region, as shown in figure 40. Calculations were run as for an unsteady, compressible flow and at full-scale Reynolds number. Surface and volume meshing was carried out using GAMBIT 2.4.6, TGRID v 14.5 and FLUENT 14.5 with the results shown in figure 41.

In order to ensure adequate accuracy, work was carried out in order to establish a reasonable level of mesh independence. Tests were conducted on three different grids of increasing cell density. The grid sensitivity tests showed that in order to capture the main features of the rotor wake with sufficient accuracy, a high mesh density must be used especially in the proximity of the blade tip and wake region. The tip mesh is shown in figure 42.

The selected CFD model comprises a total of 41.9 million cells of which $3x10^6$ are extruded prism-layer cells (around the rotor blades only) and the remaining are hexahedral with some tetrahedral cells to enable the transition between the boundary layer (prismatic) and the Cartesian grid (hexahedral). For all cases simulated the working fluid has been treated as an ideal gas and the k-ω shear-stress turbulent transport model used throughout. ISA sea-level conditions have been assumed and the dynamic viscosity has been taken as a constant of $1.789x10^{-5}$ Ns/m^2 using the value predicted by Sutherland's Law at T_{ref} = 288.15k. The fluid volume enclosed by the drum is allowed to rotate through the mesh motion option according to the rotor angular speed of 66.884rad/s while the outer fluid domain is stationary.

10.3 Results

The thrust, torque and flow field generated by the XV-15 rotor in trimmed descent, along an axial flight path passing through the VRS, have been calculated using ANSYS FLUENT 14.5. The selection of flight cases is aimed at validating the theoretical model developed previously and to investigate the nature of VRS. The C_T and C_Q time history for each case are shown below in figures 43 to 46.

The level of convergence obtained for these tests is considered to be good given the complexity and unsteadiness of the problems. Cases 3 and 4 would have required a couple more turns for the C_T and C_Q to stabilize but due to the intrinsic instability of VRS the results are considered good enough for this analysis. The FLUENT results were compared with the ADPanel simulations where the collective was adjusted to maintain a nominally constant thrust coefficient. As can be seen in figure 47, the difference of C_T between ADPanel and the CFD is constant in the region outside VRS while inside, where the rotor operates inside its own wake, the extra induced losses are not well captured by the panel code (as expected) and the difference in C_T compared to the CFD increases.

The following in figures 48 and 49 show representative contour plots of the vorticity magnitude predicted by FLUENT for cases 1, 2, 3 and 4. The flow in a longitudinal plane passing through the rotor is shown. These plots represent a snapshot of the wake structure with the rotor entering in VRS, deeply in VRS and almost in the windmill brake state.

FLUENT predicts very clear differences in the structure of the wake in the four cases. For the slow descent case (V_z/v_h = -0.4) shown in figure 50 it can be seen that the tip vortices still follow a helical-like trajectories. The flow is still periodic with some small disturbances. The vortices due to the starting solution are washed away and a smooth slipstream is still recognizable, albeit only approximately. For cases 2 (V_z/v_h = -0.8) and 3 (V_z/v_h = -1.2), the accumulation of vorticity near the rotor plane is a characteristic feature of the wake's geometry in VRS. Also apparent in the calculations is the strong recirculation of ambient vorticity through the rotor disk, mainly fed by the tip vortices and some of this vorticity originates from the earlier passage of the rotor through its own wake. Significant vorticity is generated by the blade root (case 3, figure 51) and considering the sensitivity of VRS to the surrounding flow field it is plausible that the wake vorticity originating from the inboard region could have a considerable effect on the evolution of the wake leading up to and through the VRS. Case 4 (V_z/v_h = -1.6) lies between the turbulent wake state and the windmill brake state and a more definite slipstream boundary starts to develop. The vortical structure is found to return to a more regular helical shape and the flight condition is close to the ideal autorotation point. This is calculated using the Q-criterion method for vortex identification [13].

The onset boundary of the VRS can be identified, for example, by monitoring the rotor thrust and torque fluctuations. The windowed standard deviation of the thrust and torque response of the rotor is used as an indicator of the onset of the VRS. In the figures 52 and 53, the standard deviation of the thrust and torque signal predicted by FLUENT in the last converged turn are plotted for the four cases analysed. The VRS is

accompanied by an extremely unsteady flow field surrounding the rotor. This behaviour is clearly visible with the fluctuations building up rapidly as the vertical rate of descent increases, reaching the VRS region. Thereafter, the fluctuations decrease as the rotor enters into the turbulent brake state. Cases 1, 2 and 4 show a similar trend in terms of thrust and torque fluctuations (standard deviation) while case 3 manifests much higher oscillations in thrust than torque.

Entry into the VRS manifests also as an increase in the average rotor-shaft torque (power required), which is necessary to overcome the higher induced aerodynamic losses associated with the rotor operating inside its own wake. The total power required as a function of descent velocity is presented in figure 54 showing the plateau region in correspondence of VRS.

11 COMPUTATIONAL TOOL COMPARISON

The thrust and torque generated by the XV-15 rotor has been calculated using both HMB and FLUENT by averaging the results for the converged part of the solution.

As can be seen from figures 55 and 56, there is a good level of agreement between the two CFD tools. The HMB and FLUENT calculated C_T is almost identical with a C_T of 0.008 for the slow and fast descent cases and a sudden drop to a value of 0.002 in VRS (V_z = -13.2 m/s). Torque predictions are in line for case 4 while for case 2 (deep VRS) the level of agreement between FLUENT and HMB is not perfect but not surprising, in view of the dramatic effect that the highly turbulent, chaotic and unsteady flow has on the rotor operating at this unfavourable flight condition.

12 CONCLUSIONS

This report has reviewed the main available wind tunnel and flight test data for rotors operating in vortex ring state. It was found that the VRS boundaries between the tiltrotors and the conventional helicopters were remarkably similar, in spite of a different manifestation of the instability and large differences in the rotor design. Based on the available measured data and on the corrected version of momentum theory a VRS model has been developed based on the mean convection of the tip vortices. Validation was conducted in both axial and inclined descent and good correlation was shown with the flight test data of the Dauphin SA365 helicopter and the V-22 tiltrotor. The analysis shows that the primary factor in determining the VRS boundary of a rotorcraft is disk loading and rotor efficiency.

Vortex ring state is a complex phenomenon that involves low speed wake velocities in a region with a characteristic length comparable to the rotor radius. As vortex ring state involves unsteady, large-scale vortex structure, a CFD analysis was carried out. The CFD analysis has shown that unsteady flow through the rotor causes instability and manifests as rotor thrust and torque fluctuations. A dynamic vortex that is detached from the rotor but is in vicinity of the rotor system has been seen. This combined with cross sectional cuts showing the re-ingestion of the flow by the rotor gives confidence that a VRS condition has been achieved. More importantly the correlation between steady and unsteady simulations outside of the VRS zone adds more validation to the momentum theory based VRS zone model.

13 FUTURE WORK

This paper demonstrates there is still considerable activity in research related to the VRS. The present work delivers a complete and contemporary CFD methodology that can be used to further investigate the VRS region, with a particular focus on the low speed and steep descent angles cases. Moreover, considering that significant vorticity has been observed in the blade root region, the CFD models can be improved by adding the nacelle, the spinner and the wing for a better understanding of the interactional aerodynamics and its effects on the rotor behaviour. Future work should also consider a full flight test and CFD comparison of the VRS condition to fully validate the CFD models.

14 ACKNOWLEDGEMENTS

The author gratefully acknowledges the help and support of G. Barakos and his team at the University of Glasgow. Special thanks goes to S. Gates (Leonardo Helicopters) for his time and input whilst supporting the authors with this work. This work was achieved under the HiPerTilt project [14] which was partially funded by Innovate UK.

15 REFERENCES

[1] Washizu, K.; Azuma, A.; Koo, J.; and Oka, T.: Experiments on a Model Helicopter Rotor Operating in the Vortex Ring State. Journal of Aircraft, vol. 3, no. 3, May-June 1966.

[2] J. Gordon Leishman - “Principles of helicopter aerodynamics”. Cambridge University Press, 2006.

[3] W. Johnson - "Helicopter Theory". Courier Corpporation, 1980.

[4] W. Castles Jr. and R. B. Gray - " Empirical relation between induced velocity, thrust, and rate of descent of a helicopter rotor as determined by wind-tunnel tests on four model rotors". Georgia Institute of Technology, 1951.

[5] W. Johnson - “Model for Vortex Ring State Influence on Rotorcraft Flight Dynamics". NASA Ames Research Centre, Moffett Field, California.

[6] E. Hoinville - "Etude du sillage de rotors d'elicoptere en configuration de vortex ring state". Université d’Orléans, 2007.

[7] A. Brand, R. Kisor, R. Blyth, D. Mason, C. Host - "V-22 high rate of descent (HROD) test procedures and long record analysis". The Boeing Company, Ridley Park, 2003.

[8] Steijl, R., Barakos, G.N., and Badcock, K.J., “A Framework for CFD Analysis of Helicopter Rotors in Hover and Forward Flight”, Int. J. Numer. Meth. Fluids, 51:819–847, 2006

[9] A. D'Andrea - "ADPANEL 3D unsteady full unstructured panel code coupled with a time stepping non-linear free wake vortex method". Report No. 200-90-032/04, 2006.

[10] C. W. Acree, Jr., R. J. Peyran, and W. Johnson “Rotor Design Options for Improving XV-15 Whirl-Flutter Stability Margins”, NASA/TP–2004-212262, March 2004

[11] Felker, F.F., Betzina, M.D., Signor, D.B., “Performance and Loads Data from a Hover Test of a Full-ScaleXV-15 Rotor”, NASA Technical Memorandum 86833, 1985

[12] Ladson, C.L., and Brooks, C.W., Jr., “Development of a Computer Program to Obtain Ordinates for NACA 6- and 6A-Series Airfoils,” NASA TM X-3069, Sept., 1974

[13] Jeong, J., Hussain, F., “On the Identification of a Vortex”, Journal of Fluid Mechanics, Vol. 285, pp69-94, 1995

[14] Garcia-Duffy, C., "Innovative Aerodynamic Design Solutions for High-Performance Tiltrotor Aircraft - HiPerTilt (Second Level Project Plan)", Issue 2, TSB Ref. 101370, Feb 2013

Authors	Test date	No. of blades	Radius [ft]	RPM	Twist [deg]	Solidity	Flight condition	Facility
Castles and Gray	1951	3	2,3	1200, 1600	0, -12	0.05	Axial	Wind-tunnel, 9ft
Taghizad	2002	4	19.6	319.6	-10	0.083	Axial, inclined	Flight test, Dauphin
V-22 IIT	2003	3	19	397	-38	0.105	Axial, inclined	Flight test, V-22

Table 1: Main test campaigns on rotors in vortex ring state.

Bell XV-15 Tiltrotor			
Case No.	Aircraft Mass [kg]	Density altitude [ft] - [m]	
1	4600	3280	1000
2	4600	6561	2000
3	4600	16404	5000
4	6000	3280	1000
5	6000	6561	2000
6	6000	16404	5000

Table 2: XV-15 aircraft configurations that have been used to test the VRS theoretical model.

Bell XV-15 Tiltrotor			
Case No.	Aircraft Mass [kg]	Density altitude[m]	Induced power factor, ki
7	6000	1000	1.0, ideal
8	6000	1000	1.15

Table 3: Induced power factor influence on the XV-15 VRS envelope

Number of blades	3
Rotor diameter	7.62 m
Blade chord	0.356 m
Rotor solidity ratio	0.0891
Blade twist	-42 deg (non-linear)
Blade precone angle	2.5 deg
Rotor aerofoils	NACA 64-series

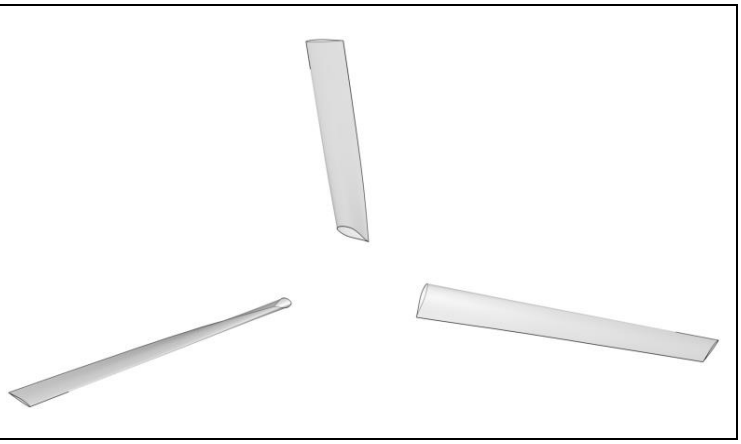


Table 4: Rotor system characteristics

Case No.	Pitch (°)	V_z (m/s)	V_x (m/s)	C_T ADPanel	η
1	8.4	-6.6032	0	0.00997	-0.4
2	7.2	-13.2064	0	0.00728	-0.8
3	5.6	-19.8096	0	0.01020	-1.2
4	4.3	-24.7620	0	0.01112	-1.5

Table 5: Steady simulation inputs

Case No.	Pitch (°)	V_z (m/s)	V_x (m/s)
Slow Climb	11.2	6.6032	0
VRS	7.2	-13.2064	0
Fast Descent	4.3	-24.7620	0

Table 6: Unsteady simulation input data

Case No.	Pitch (°)	Vz (m/s)	Vx (m/s)	η (V_z/V_h)
1	8.4	-6.6032	0	-0.4
2	7.2	-13.2064	0	-0.8
3	5.6	-19.8096	0	-1.2
4	3.8	-26.4128	0	-1.6

Table 7: CFD cases of the XV-15 in axial flight

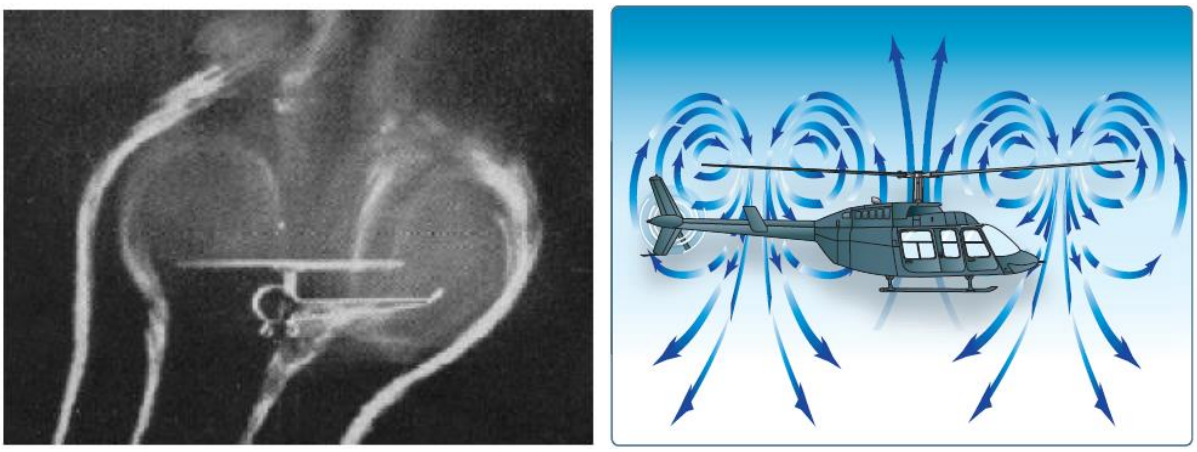


Figure 1: Flow visualization at the rotor operating in VRS from Drees and Hendal 1951 (left) and a vortex ring state simplified illustration (right).

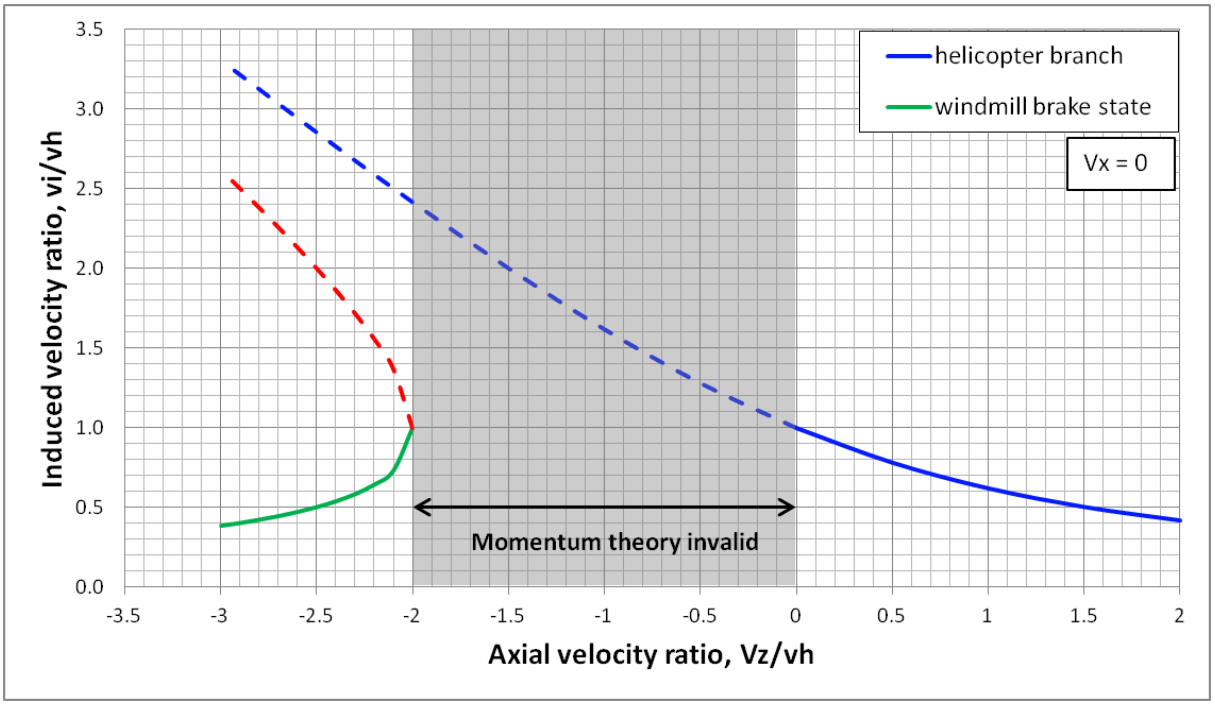


Figure 2: Induced velocity model from momentum theory in axial vertical flight.

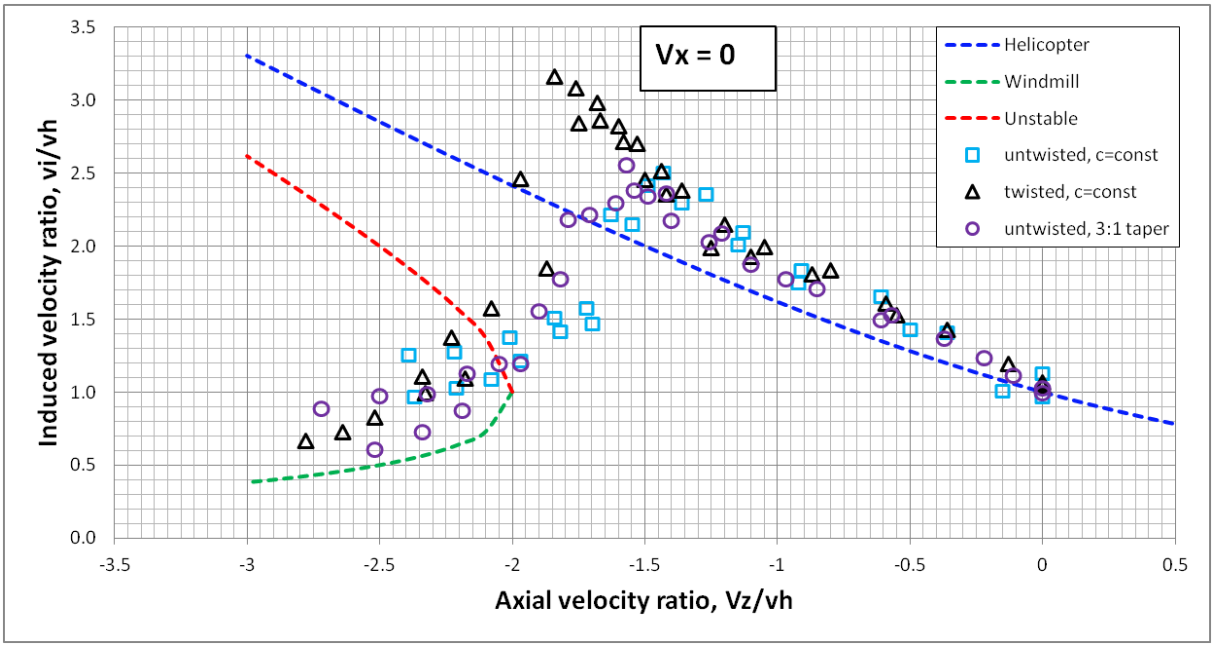


Figure 3: Induced velocity theoretical model against Castles and Gray experimental results.

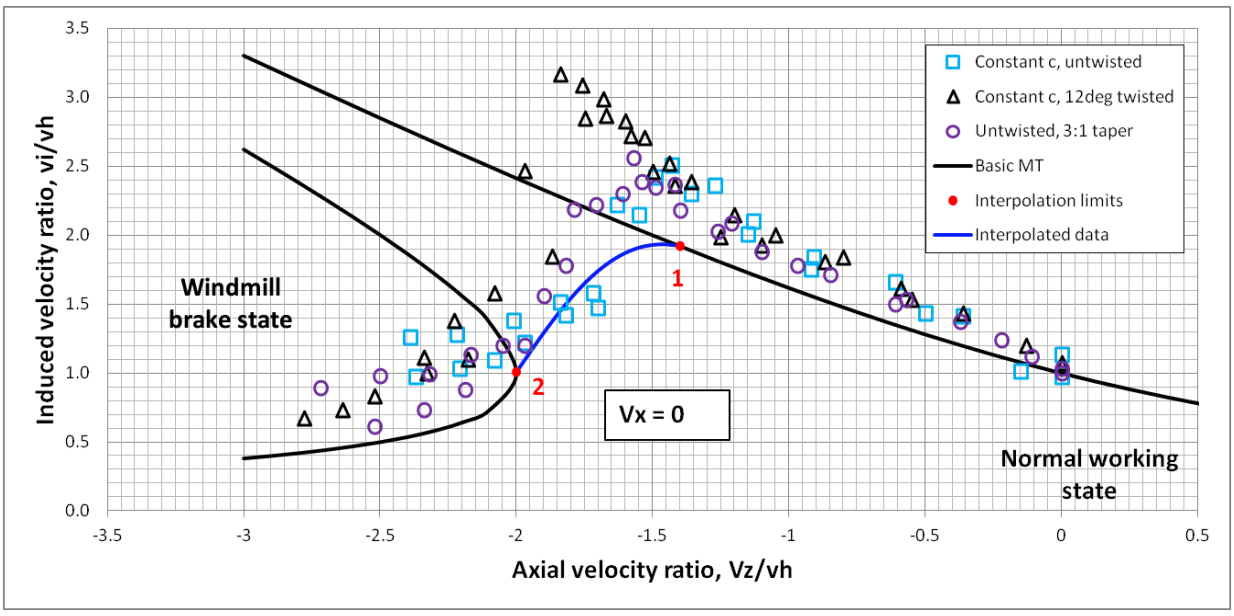


Figure 4: Extended momentum theory vs Castles and Gray experimental results.

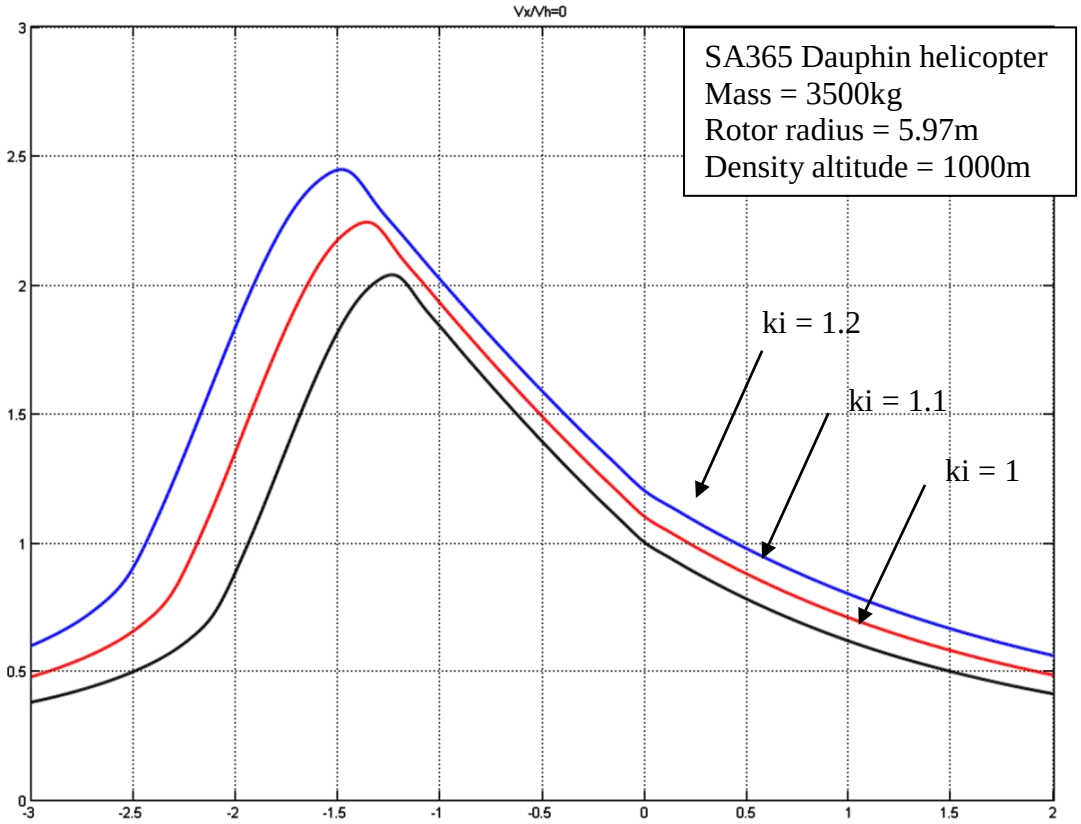


Figure 5: Induced flow curves from the corrected momentum theory as a function of the induced power factor, k.

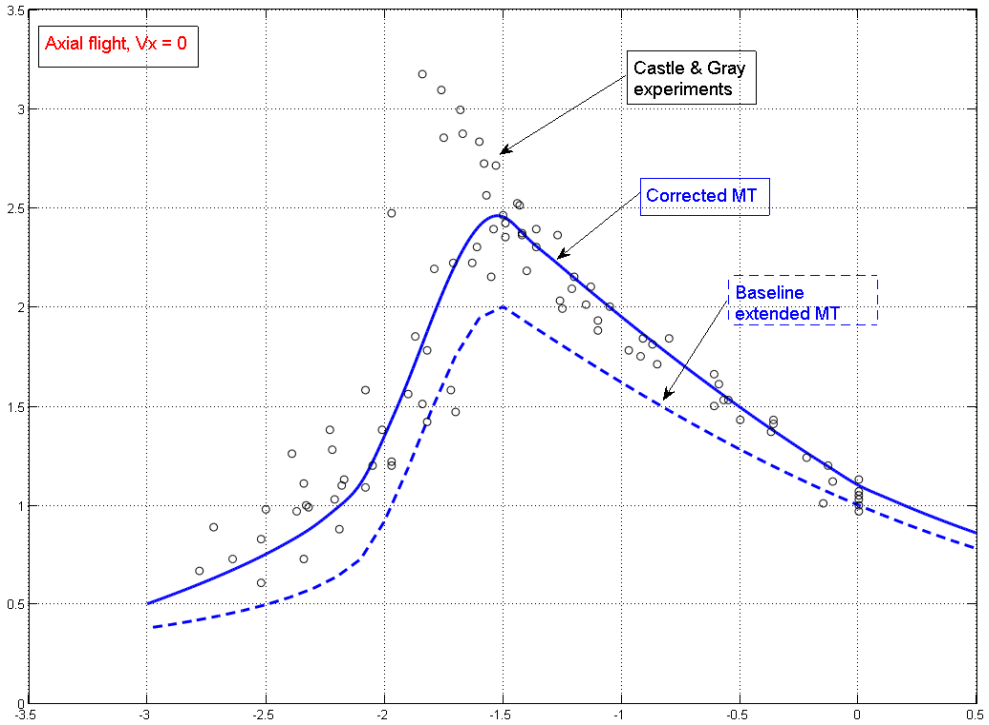


Figure 6: Induced velocity comparison between the baseline extended model, the corrected model and Castles and Gray experimental data.

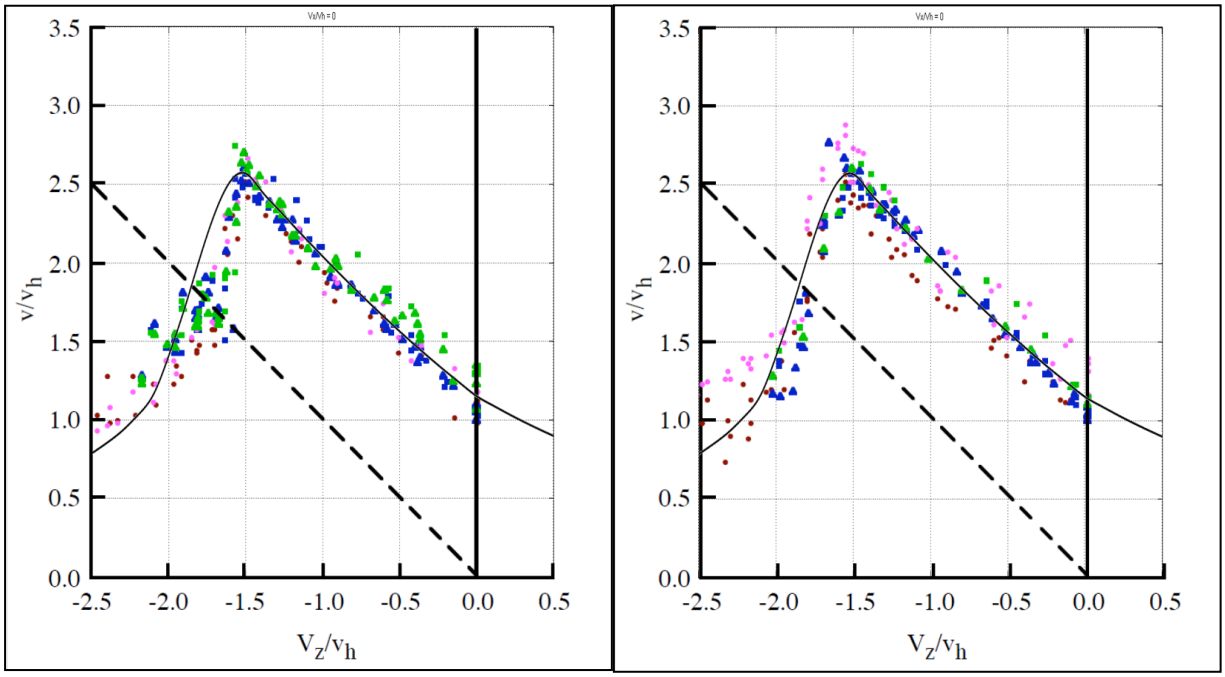


Figure 7: axial flow, σ = 0.05, θ_{tw} = 0, constant chord (L); axial flow, σ = 0.05, θ_{tw} = 0, 3:1 taper (R).

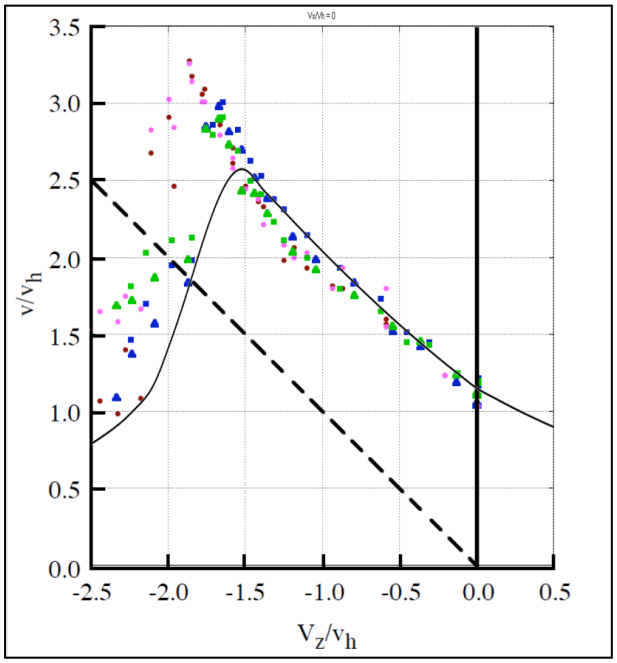


Figure 8: axial flow, σ = 0.05, θ_{tw} = -12deg, constant chord.

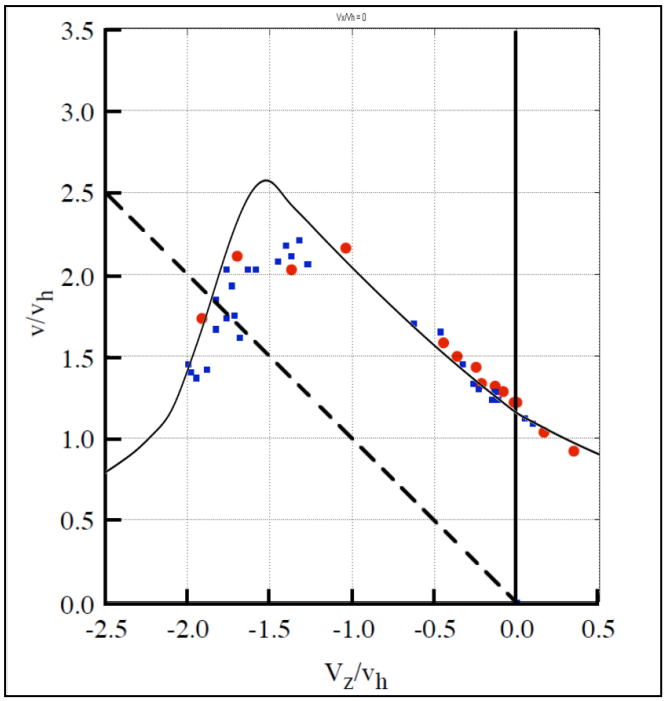


Figure 9: axial flow, σ = 0.083, θ_{tw} = -10deg, Dauphin AS365 helicopter.

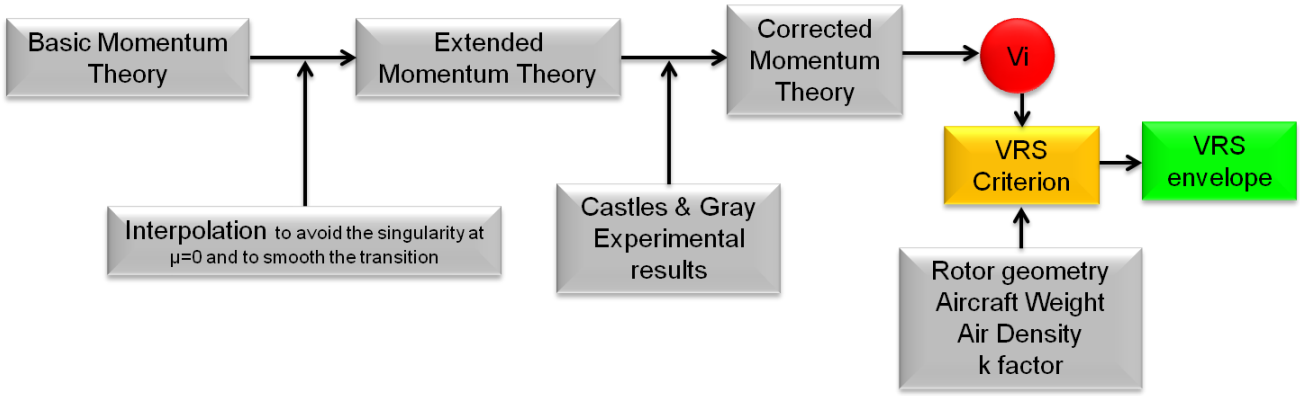


Figure 10: schematic representation of the Matlab® routine.

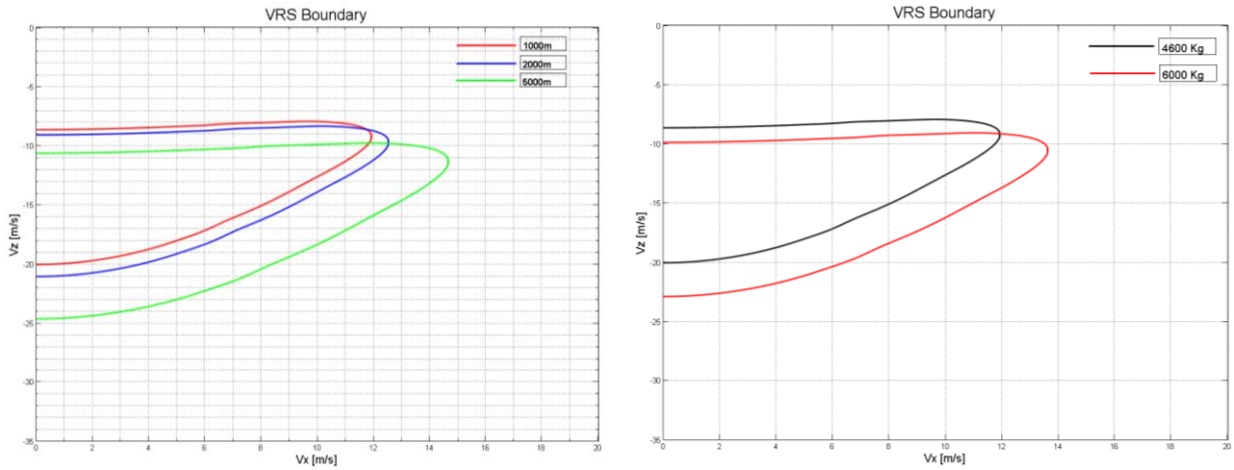


Figure 11: XV-15 VRS boundary influence of density altitude at Mass 4600 kg (L); VRS boundary influence of aircraft mass at density altitude 1000m (R).

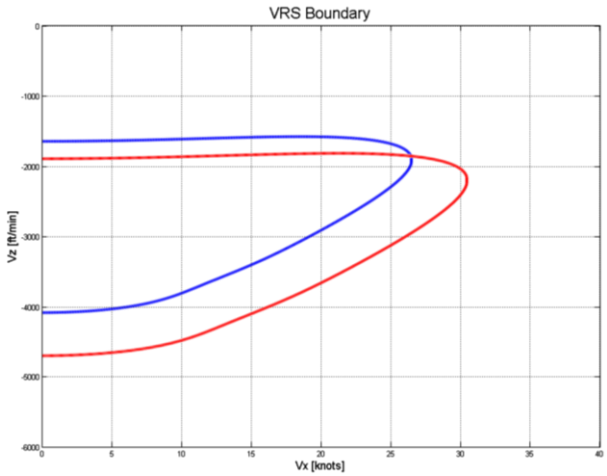


Figure 12: XV-15 VRS boundary, influence of the induced power loss factor k



Figure 13: Aérospatiale SA 365 Dauphin flight tests at CEV.

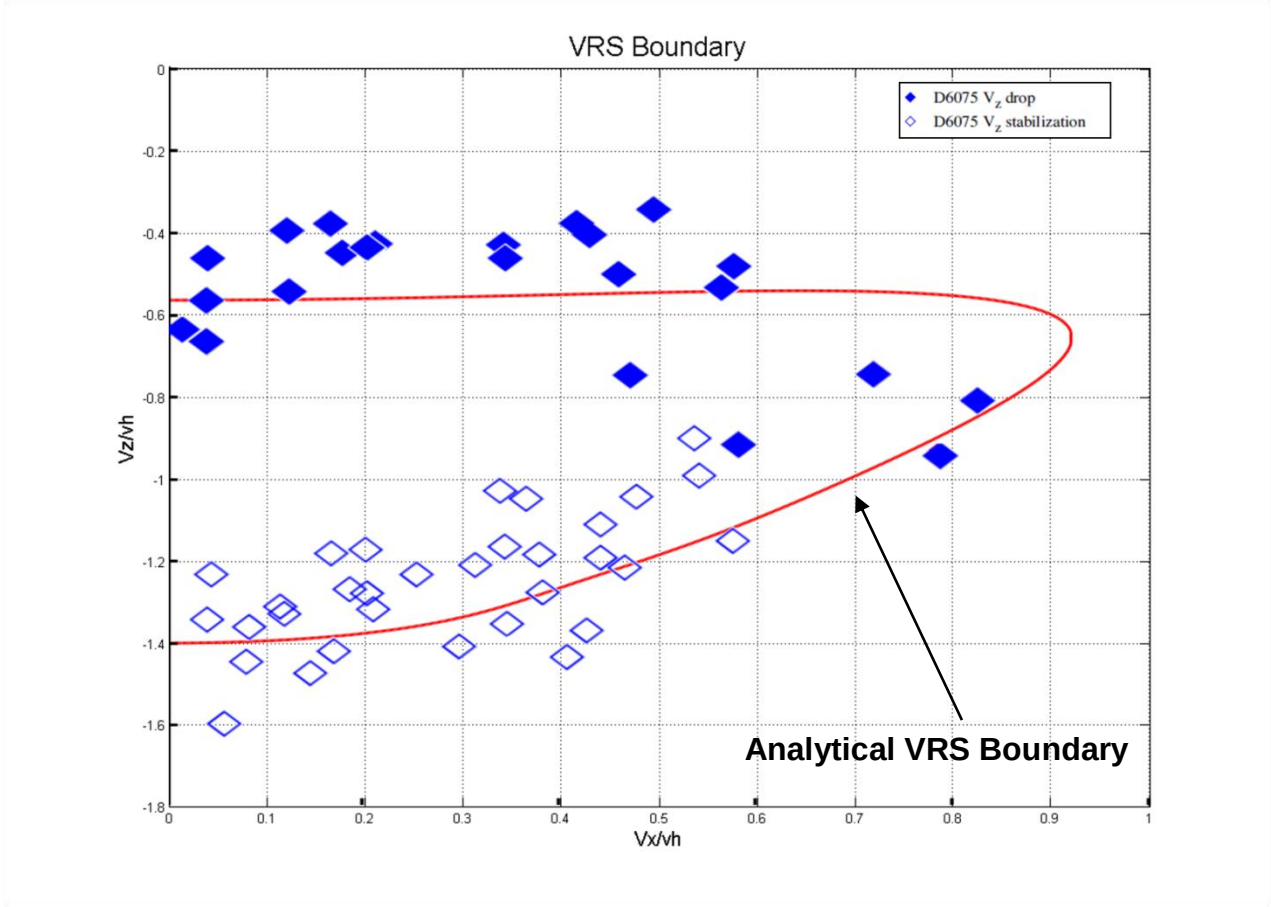


Figure 14: SA365 Dauphin helicopter test data compared with the VRS boundary from the analytical model.

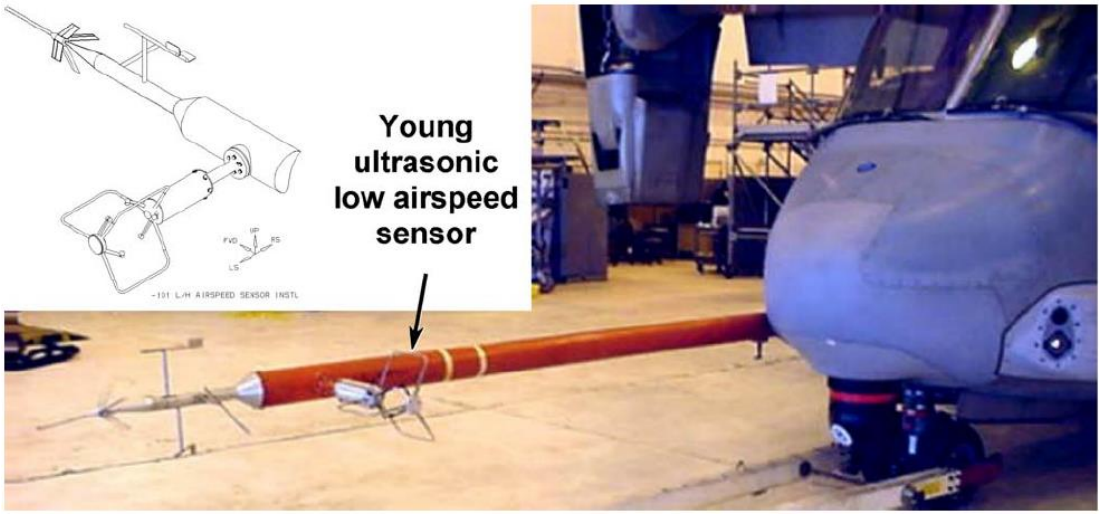


Figure 15: Boom-mounted anemometer used to provide more accurate velocity readings in high rate of descent regime.

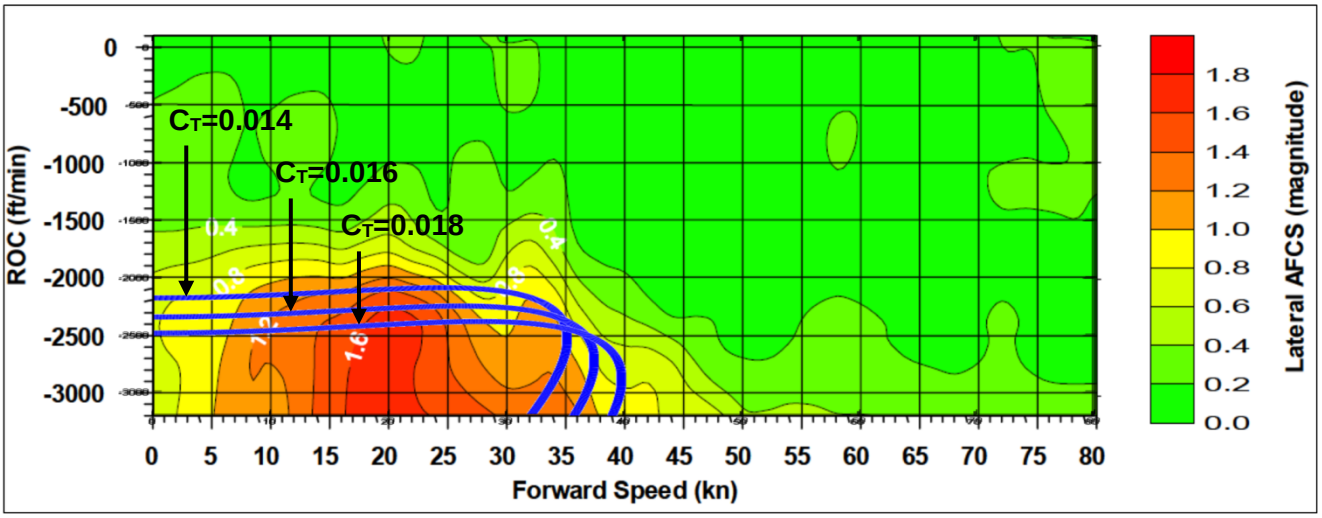


Figure 16: The theoretical VRS boundaries for CT = 0.014, 0.016, and 0.018 against Lateral AFCS from flight tests.

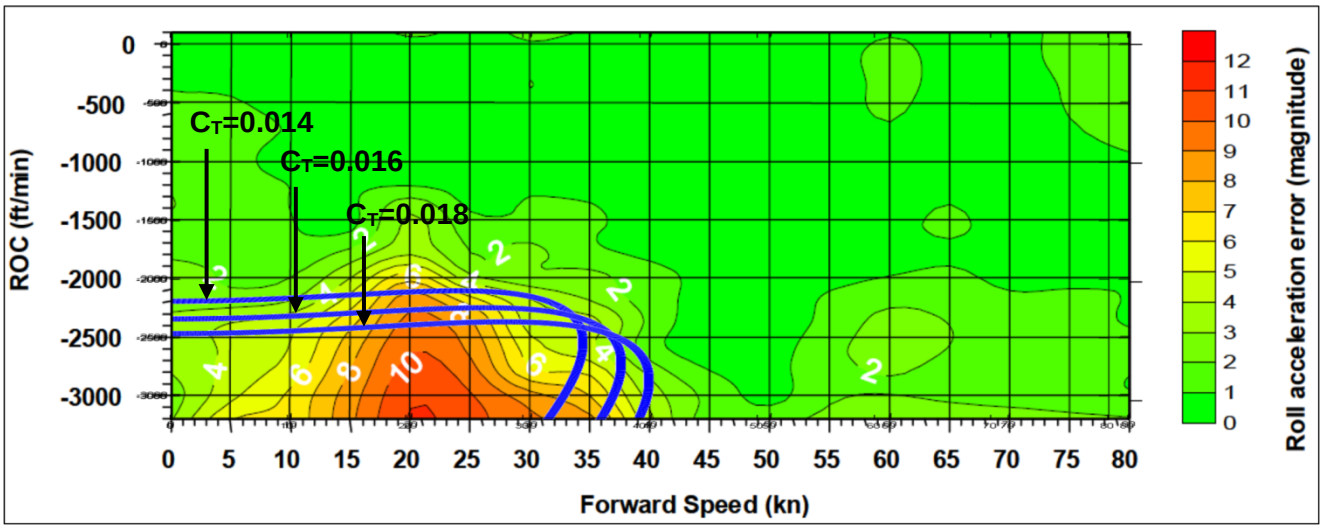


Figure 17: The theoretical VRS boundaries for CT = 0.014, 0.016 and 0,018 against roll acceleration error measured during flight tests.

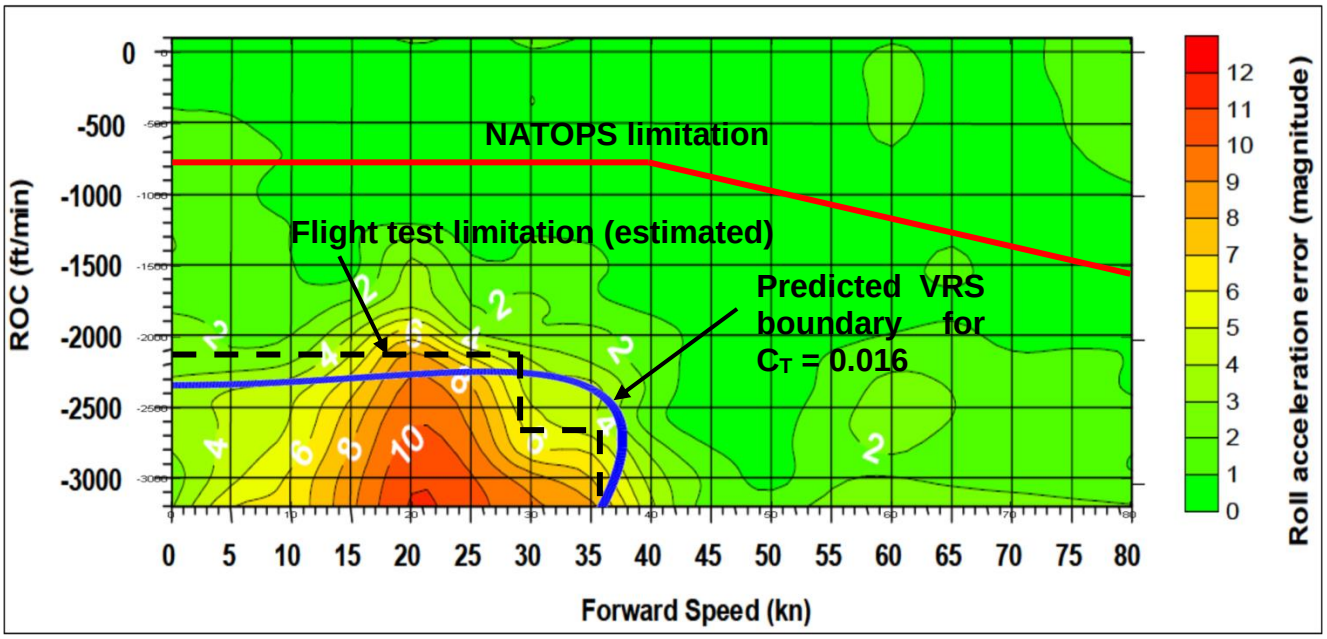


Figure 18: VRS boundaries from flight tests, corrected momentum theory and NATOPS.

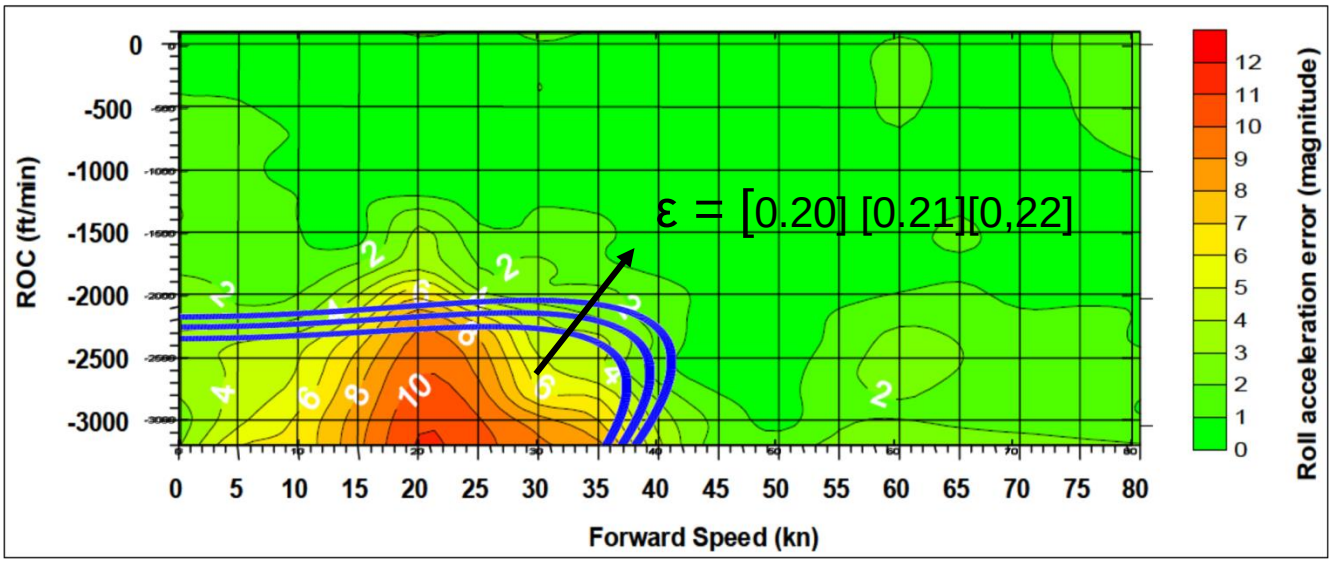


Figure 19: Theoretical model sensitivity to the wake critical transport velocity ε.

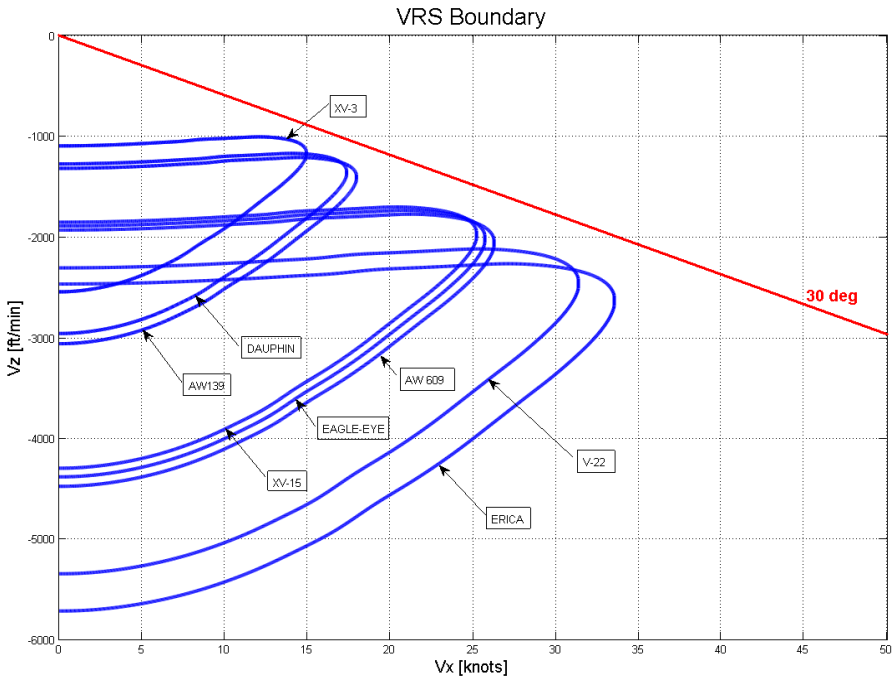


Figure 20: VRS boundaries for different rotorcraft models. Typical take-off weights are from published data, ISA sea level conditions.

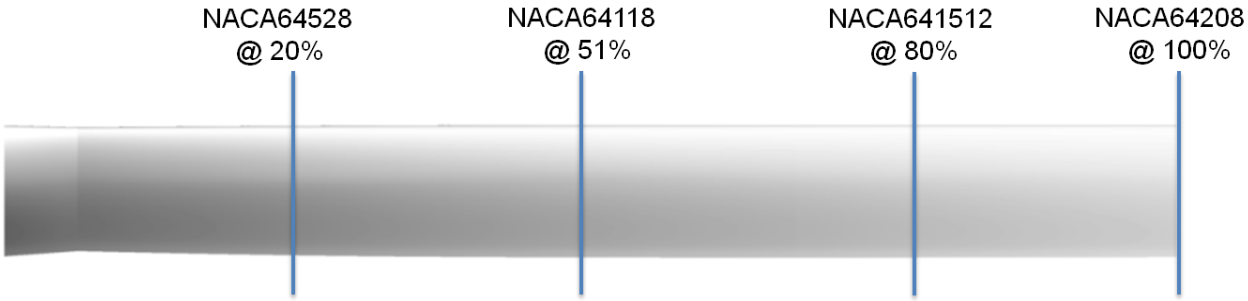


Figure 21: CATIA® generated XV-15 blade

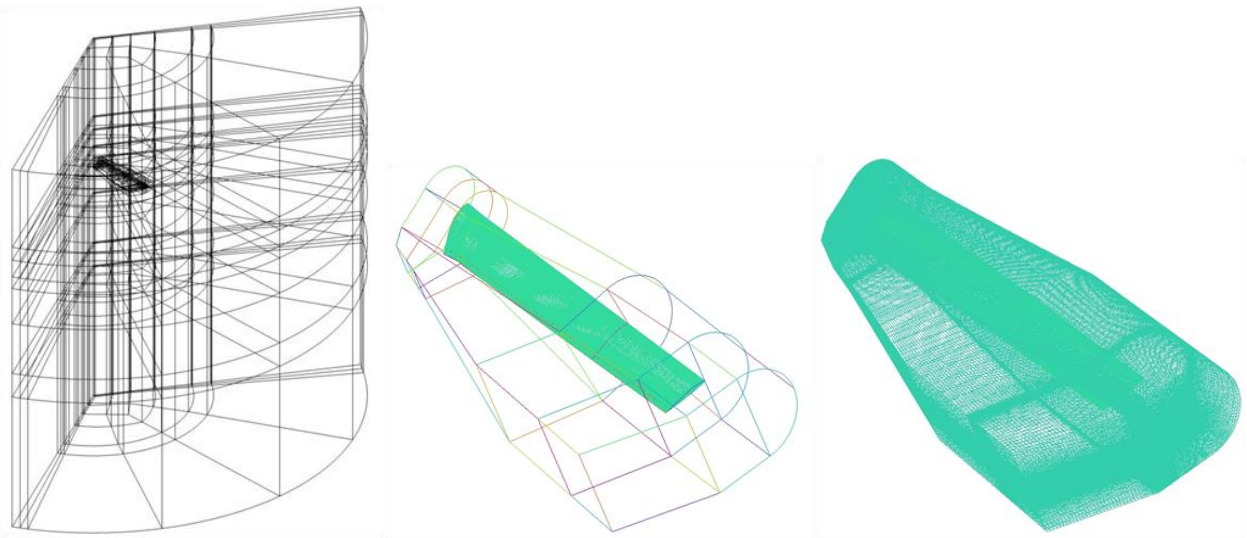


Figure 22: Steady HMB mesh of XV-15 rotor using chimera

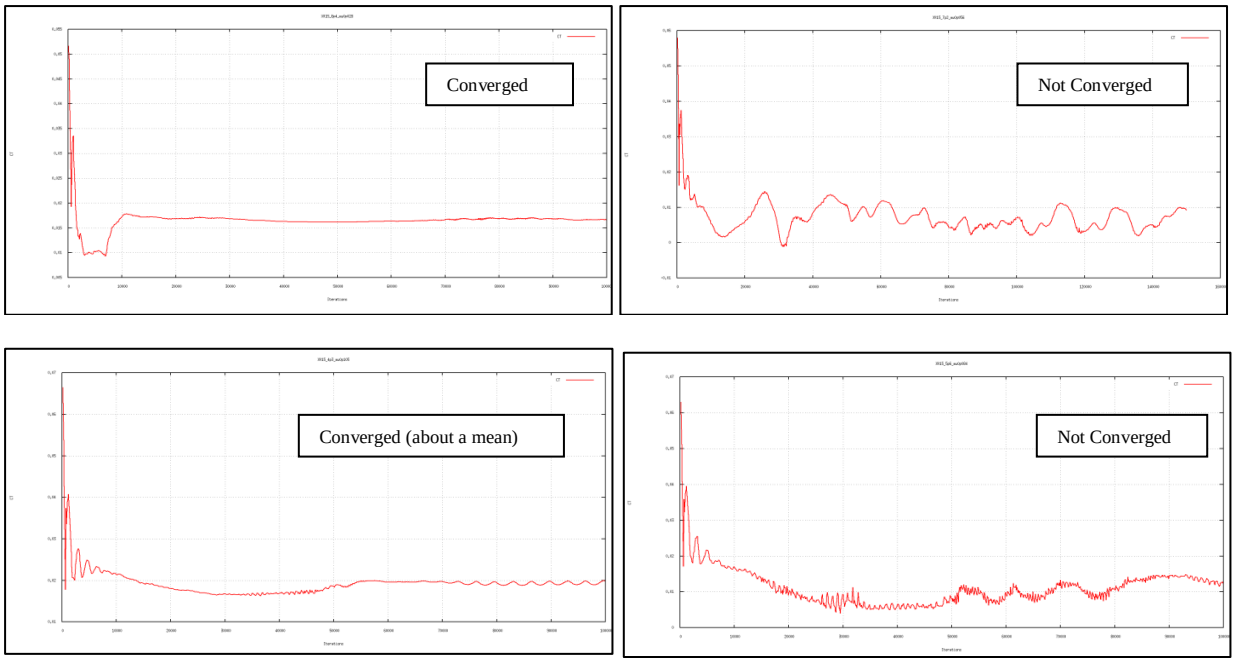


Figure 23 - Ct convergence history of the steady simulations. Clockwise from top left, simulations are case 1, 2, 3 and 4.

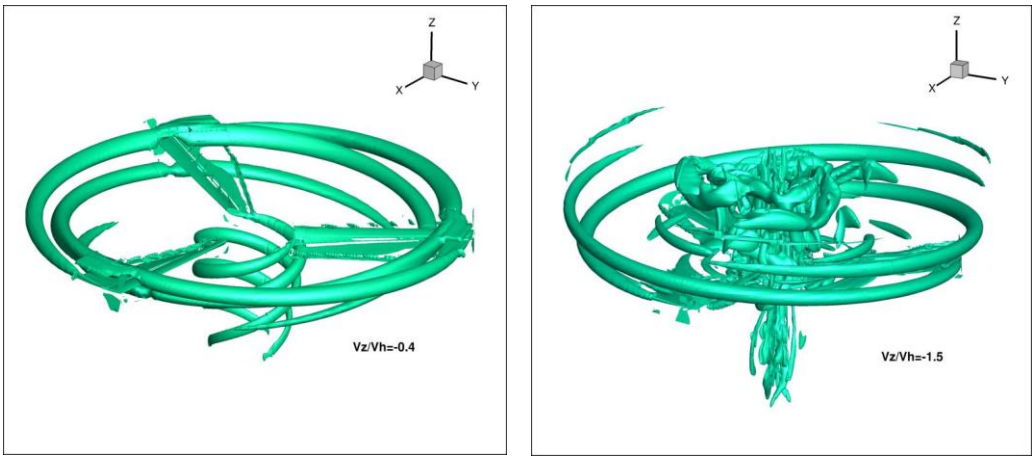


Figure 24 - Case 1 (L) and case 4 (R), which are both outside the VRS region

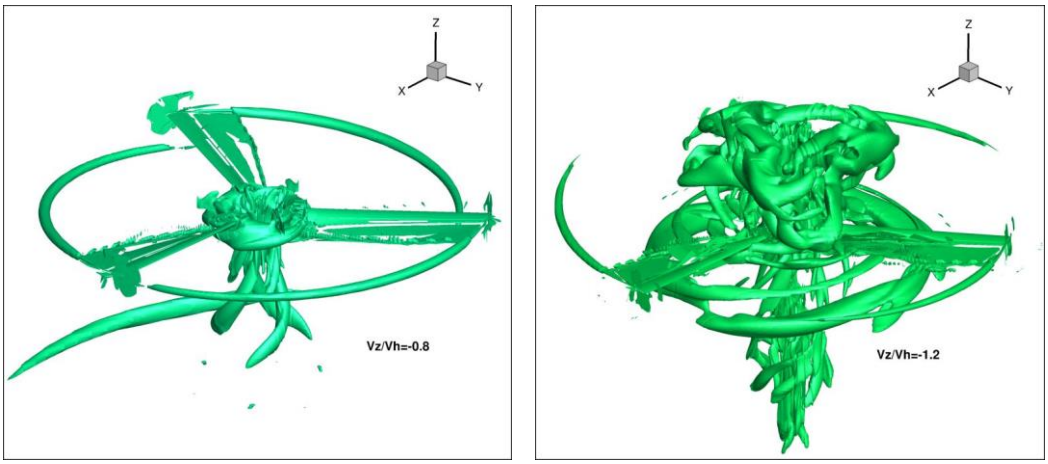


Figure 25 - Case 2 (L) and case 3 (R), which are both inside the VRS region

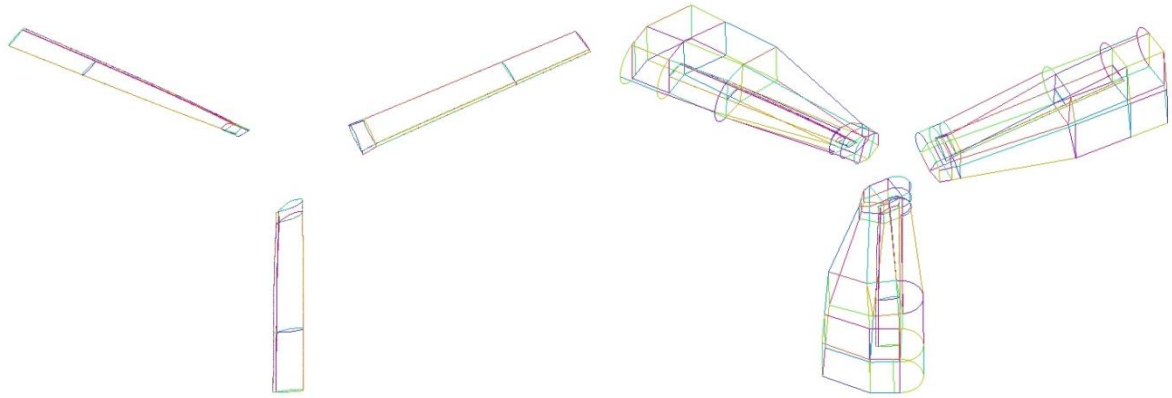


Figure 26 - XV-15 rotor blades without and with chimera bounding boxes

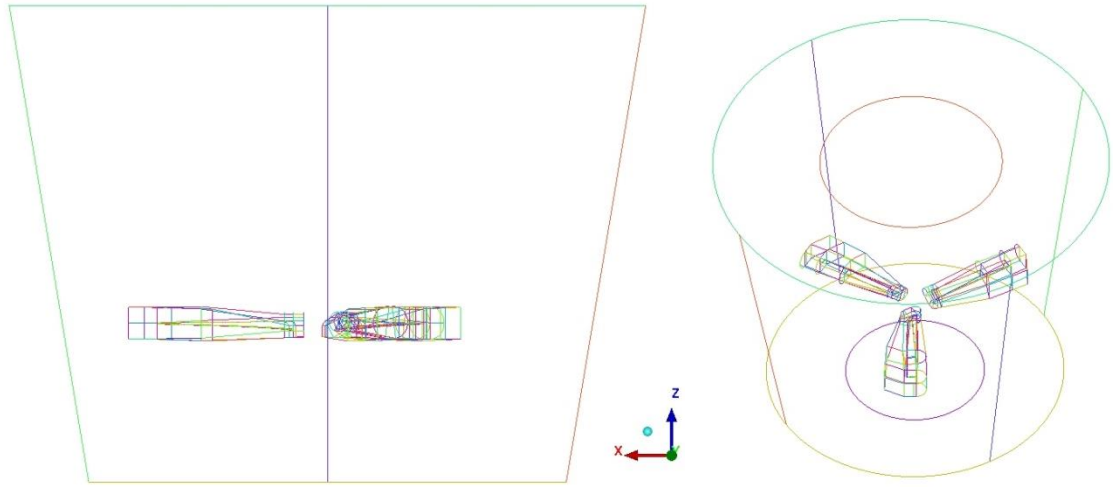


Figure 27 - New VRS "bucket" bounding box

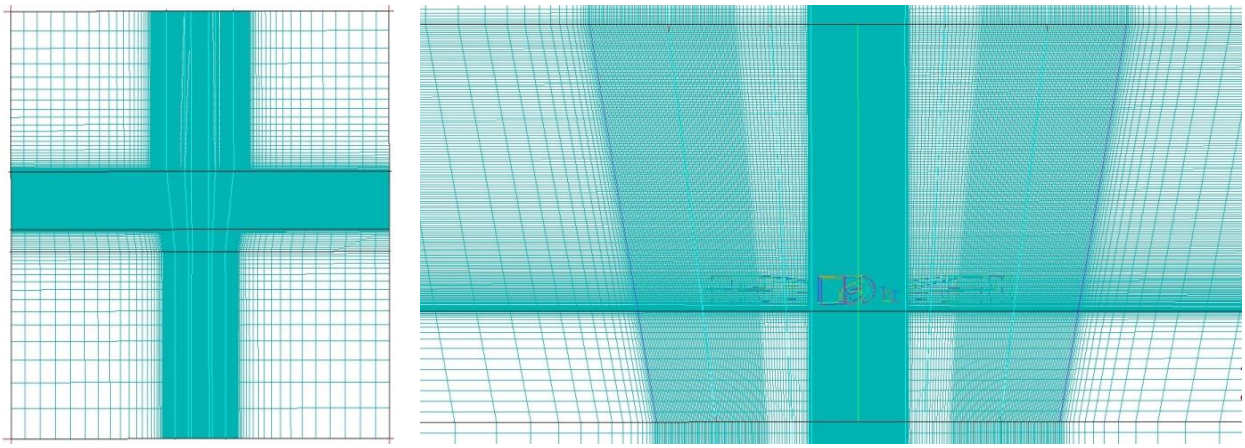


Figure 28 - VRS mesh from side including close up of where the rotor system sits

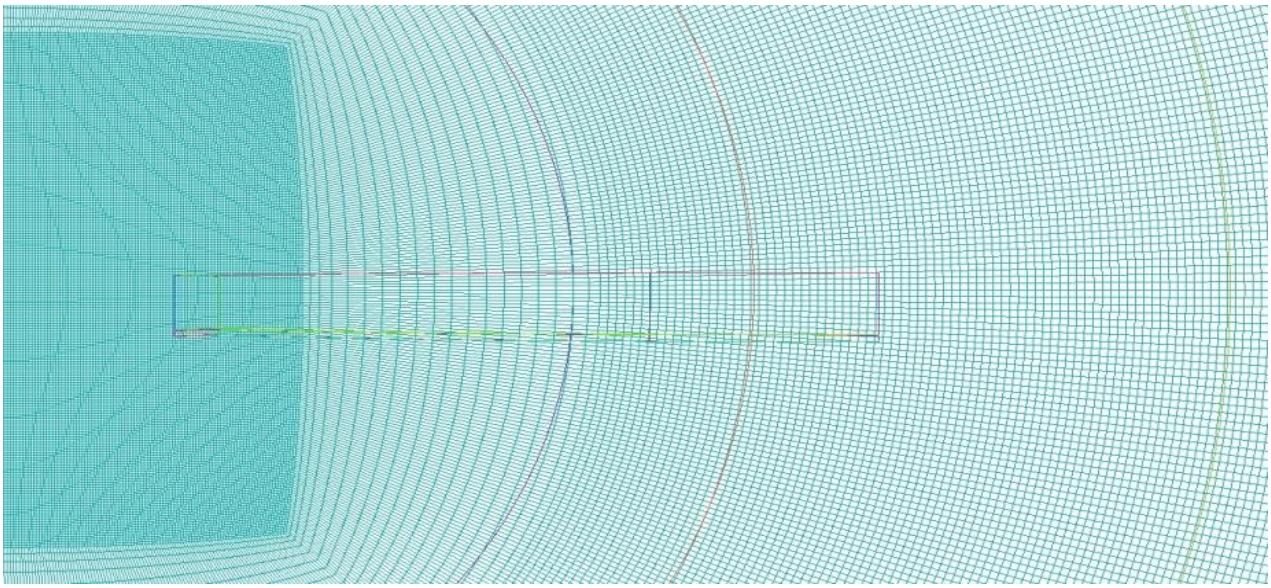


Figure 29 – Top down view of the VRS mesh

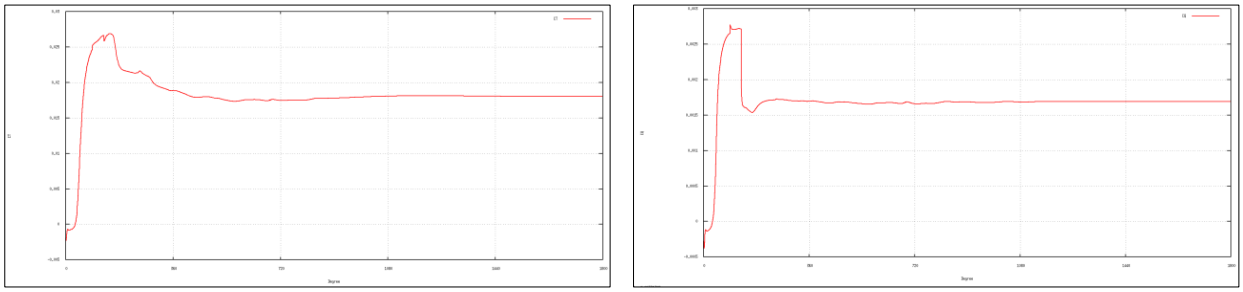


Figure 30 - Slow Climb C_T and C_Q against Degrees

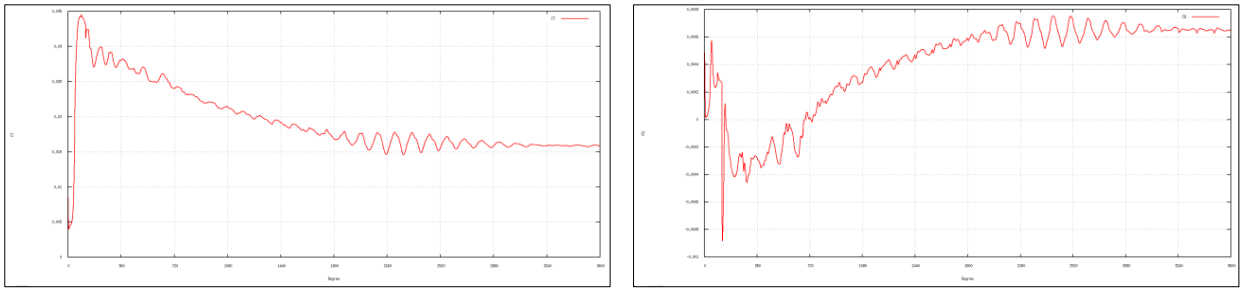


Figure 31 - Fast Descent C_T and C_Q against Degrees

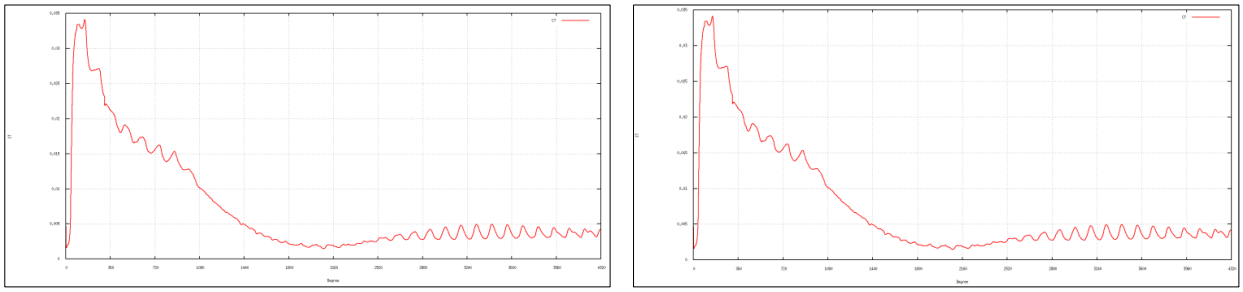


Figure 32 - VRS C_T and C_Q against Degrees

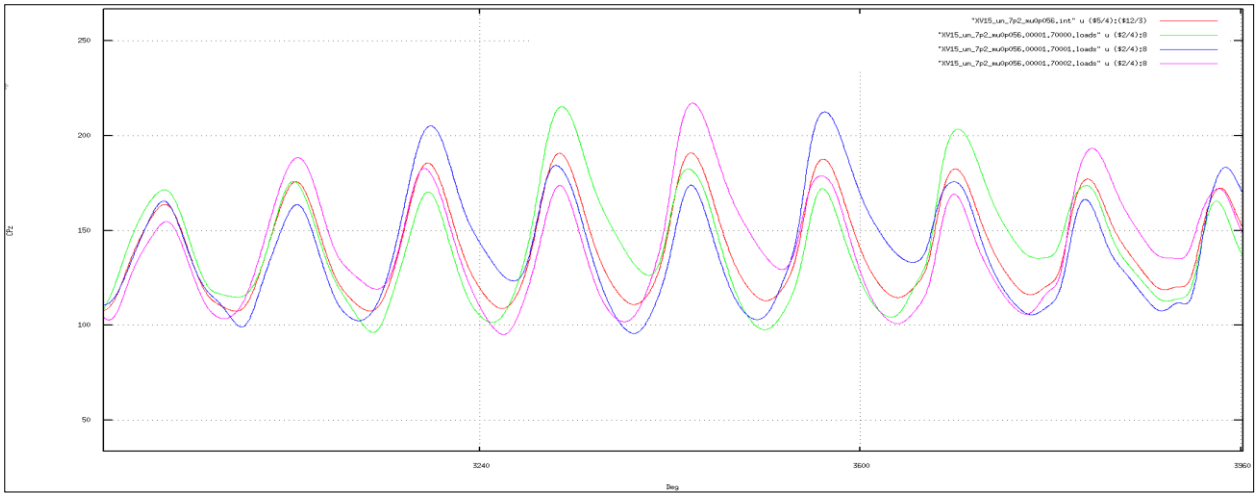


Figure 33 - Close up of forces across the 3 blades with the mean value in red

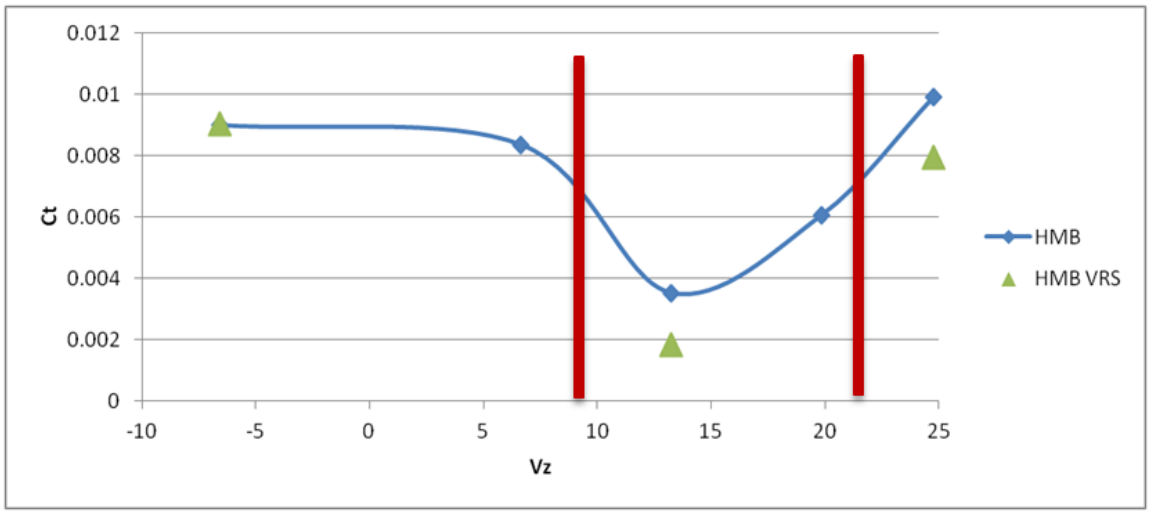


Figure 34: Thrust coefficient comparison against vertical speed

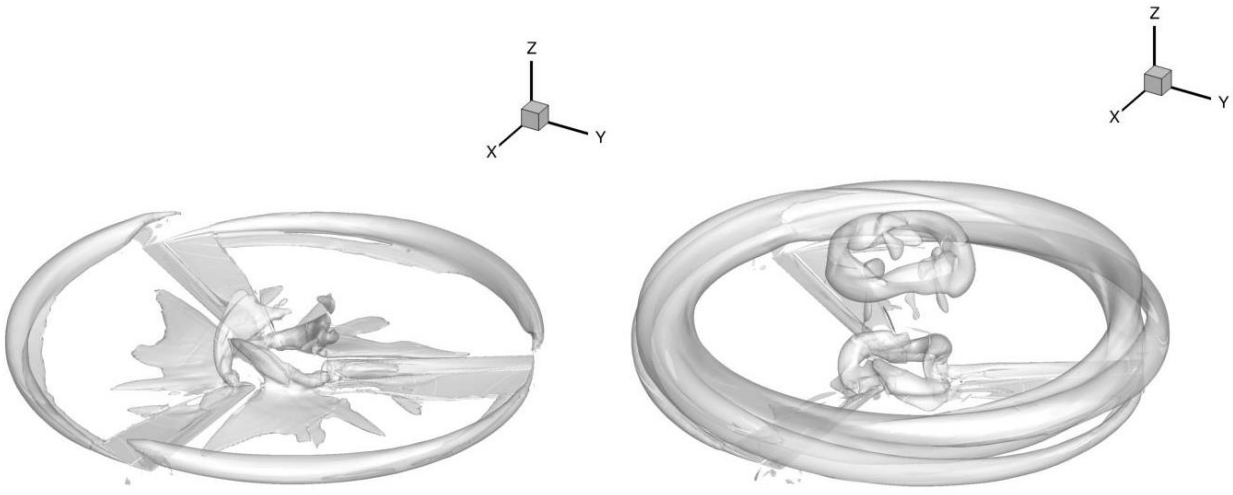


Figure 35 - Wake images of first and second turns (1 turn = 360°)

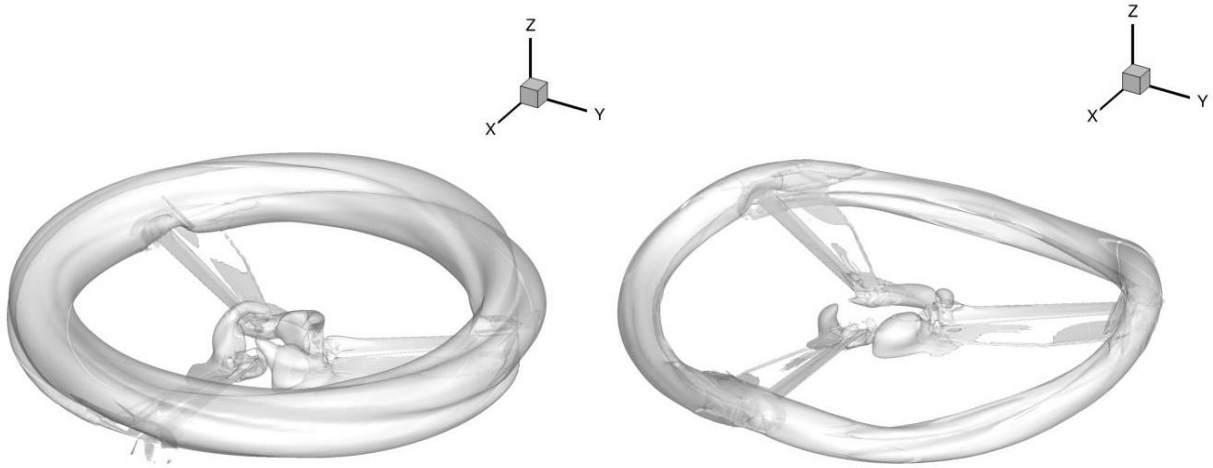


Figure 36 - Wake images of fourth and eighth turns

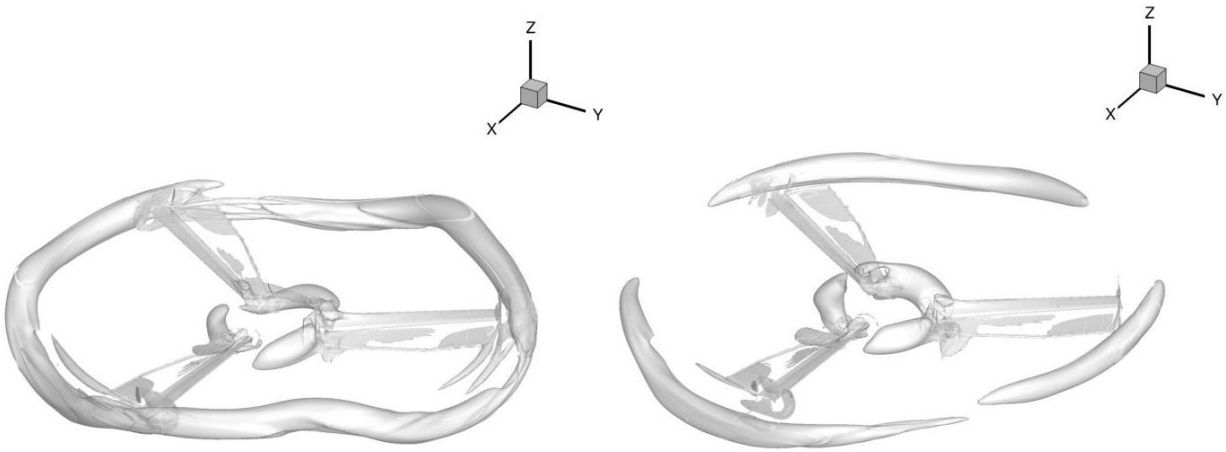


Figure 37 - Wake images of tenth and twelfth turns

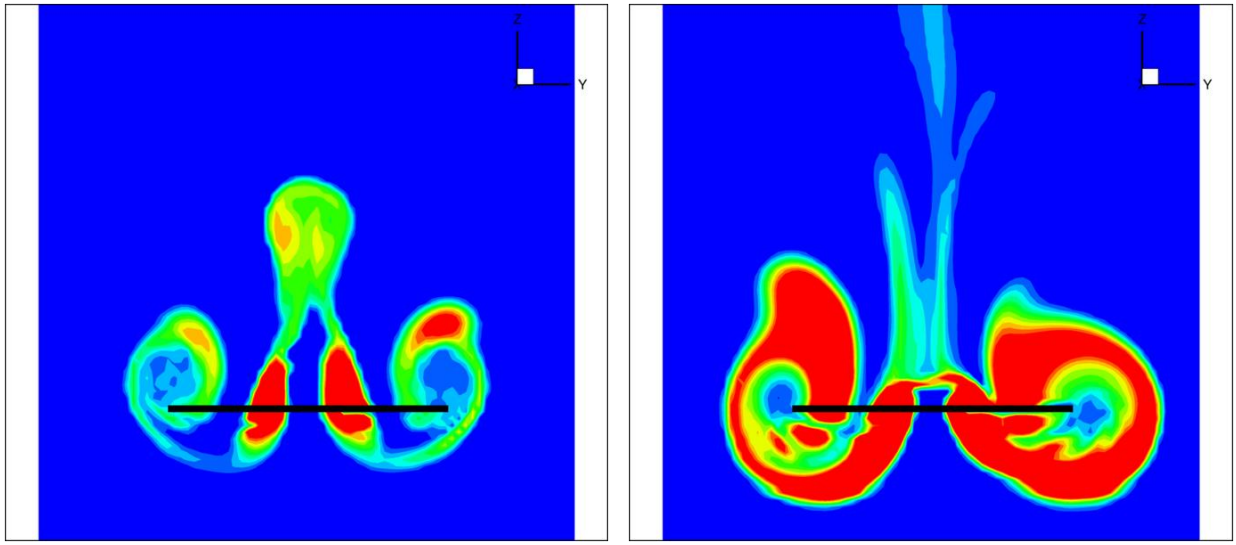


Figure 38 - Cross section of rotor system showing turbulence intensity at 4 turns (left) and 10 turns (right).

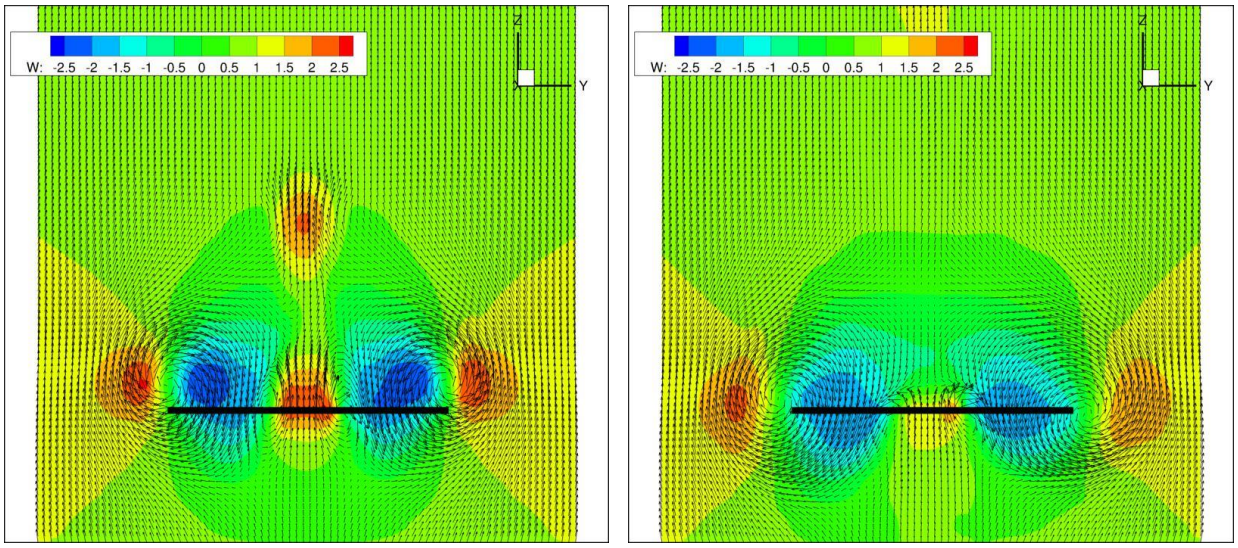


Figure 39 - Cross section of rotor system showing vertical velocity with vectors at 4 turns (left) and 10 turns (right).

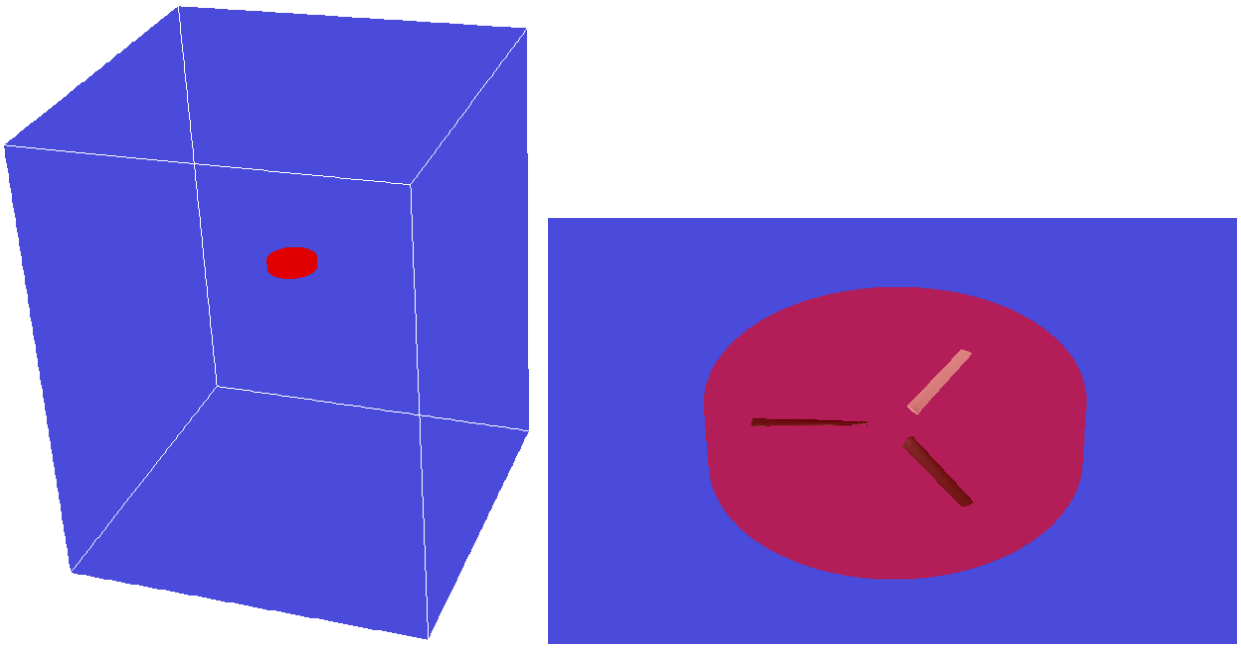


Figure 40: FLUENT model with background block (L) and foreground drum containing rotor system (R)

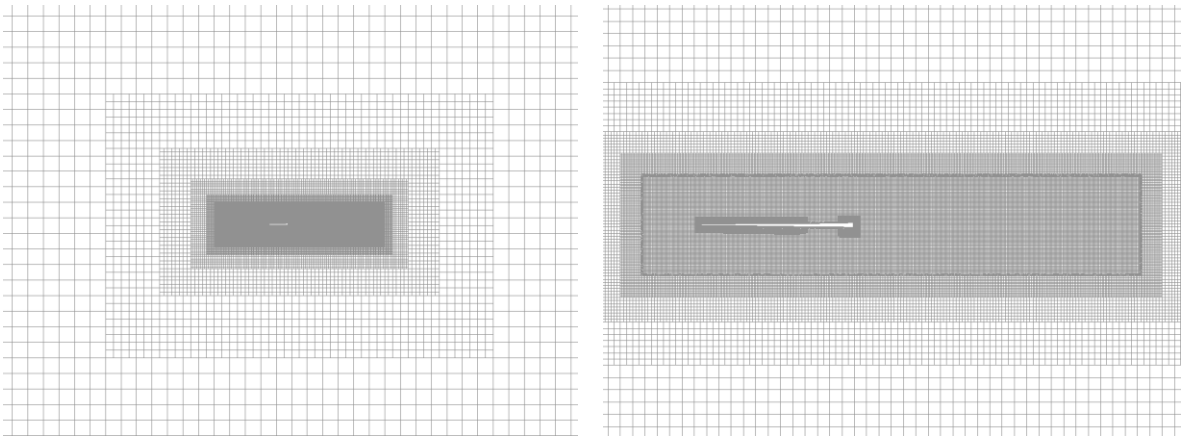


Figure 41: Bounding box mesh showing drum and refinement

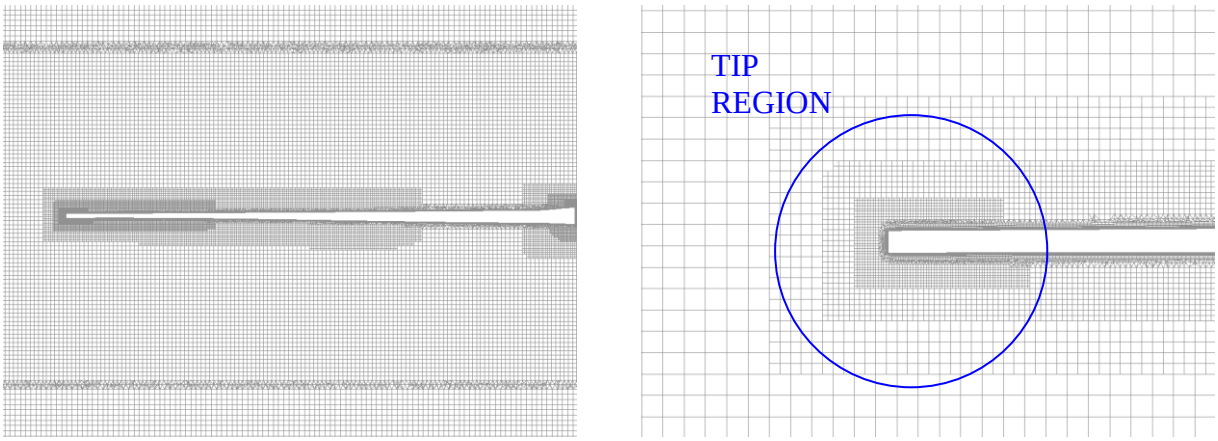


Figure 42: Close-up view of the blade (left) and the tip region (right).

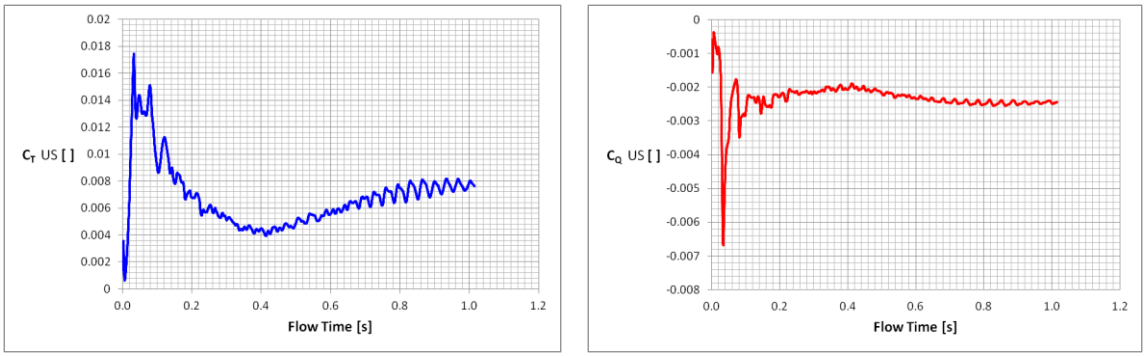


Figure 43: CT and CQ time history for case1 (slow descent)

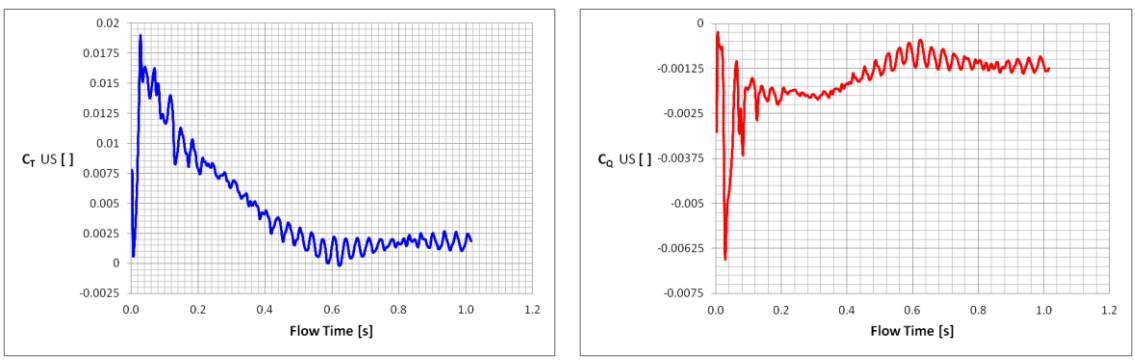


Figure 44: CT and CQ time history for case2 (VRS-1)

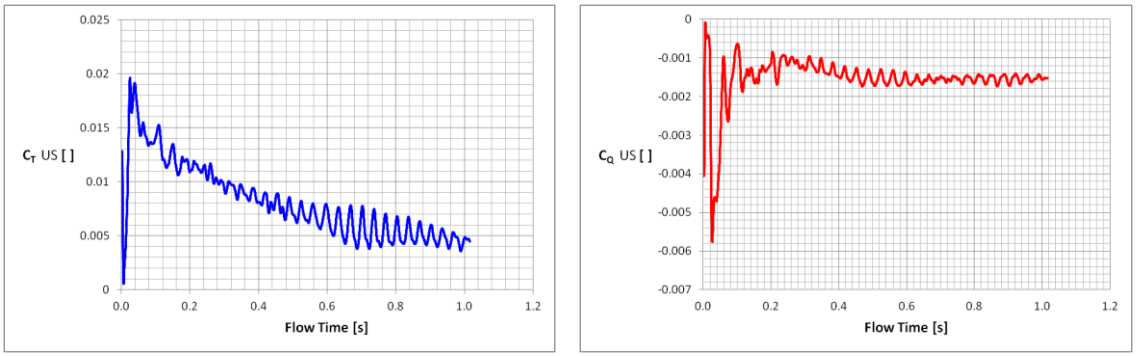


Figure 45: CT and CQ time history for case3 (VRS-2)

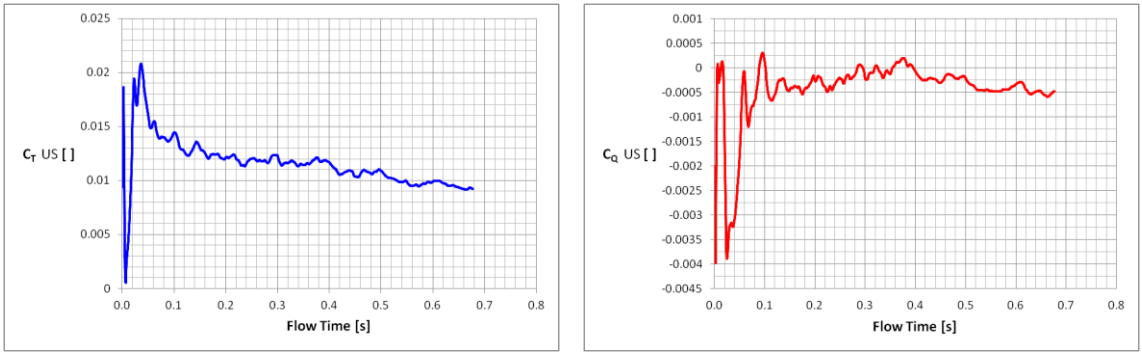


Figure 46: CT and CQ time history for case4 (fast descent)

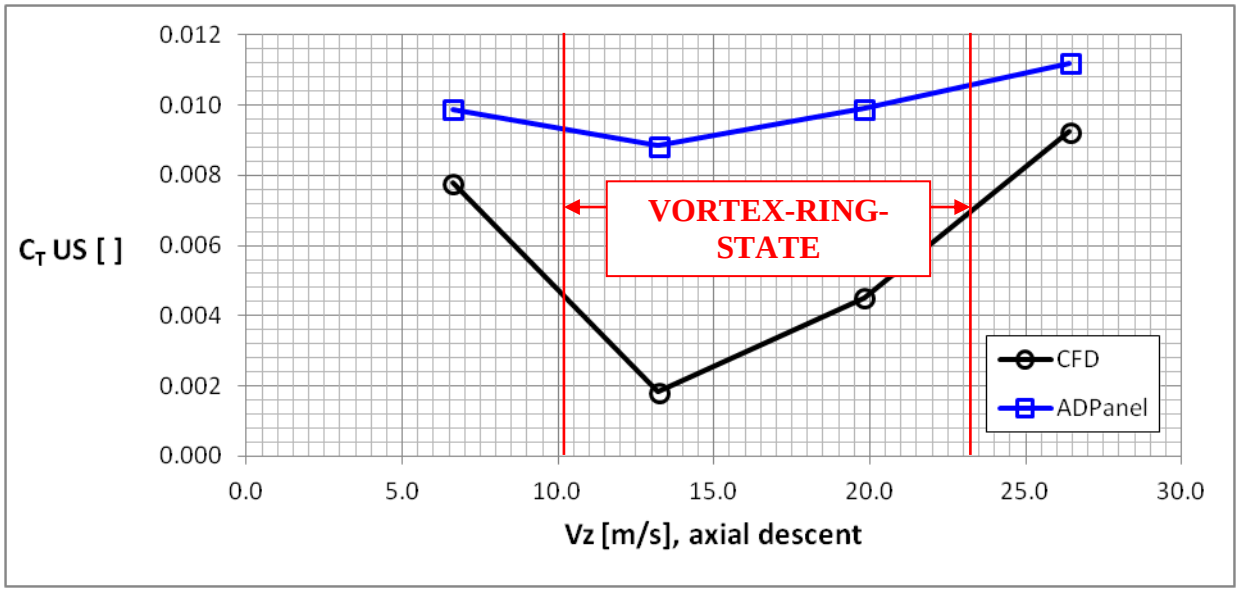


Figure 47: CT against descent velocity; ADPanel vs CFD

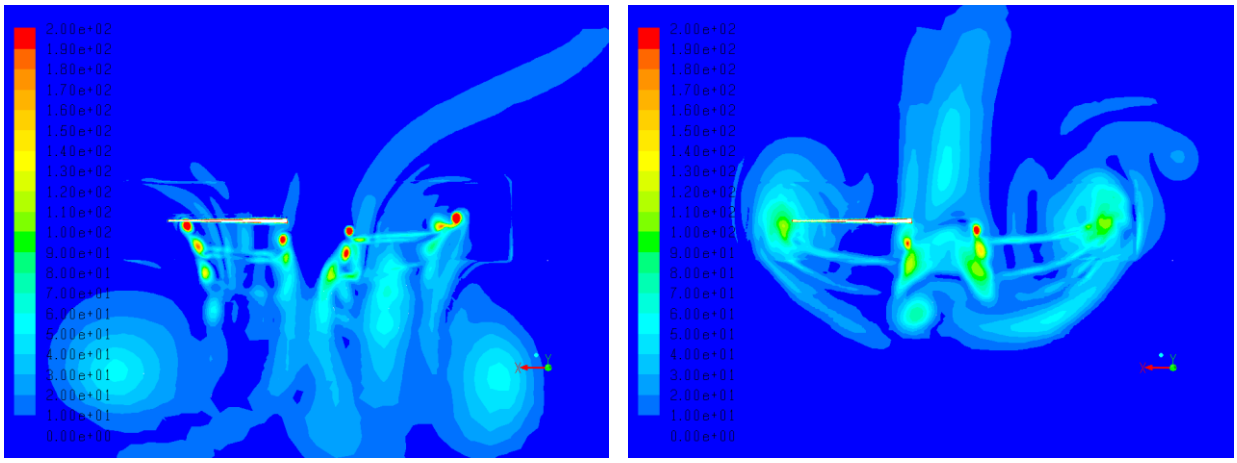


Figure 48: Vorticity distribution in a longitudinal plane surrounding the rotor in descending flight. Case1, Vz = -6.6032 m/s CT = 0.0078 (L) and Case2, Vz = -13.2064 m/s CT = 0.0018 (R)

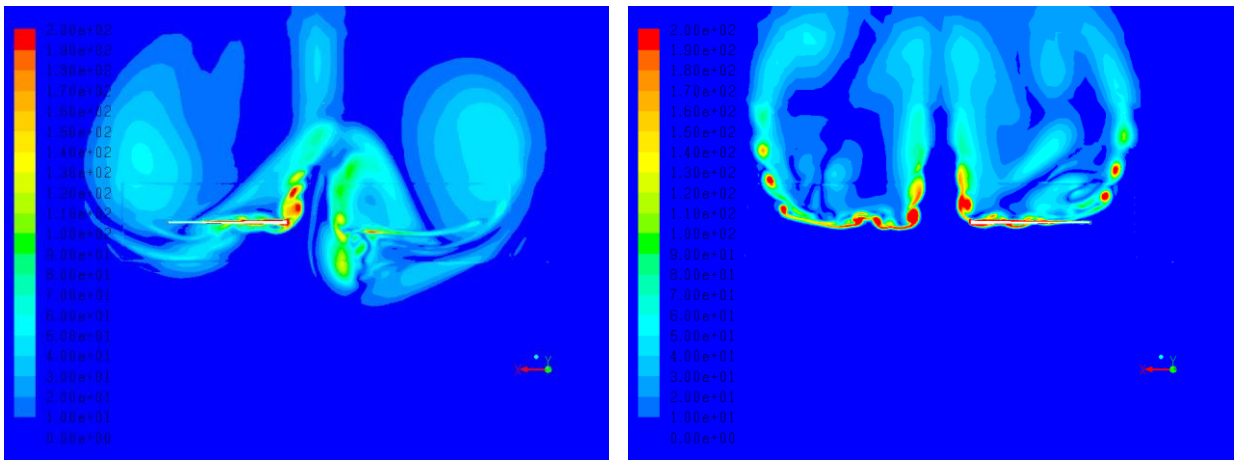


Figure 49: Vorticity distribution in a longitudinal plane surrounding the rotor in descending flight. Case3, Vz = -19.8096m/s CT = 0.0045 (L) and Case4, Vz = -26.4128m/s CT = 0.0092 (R)

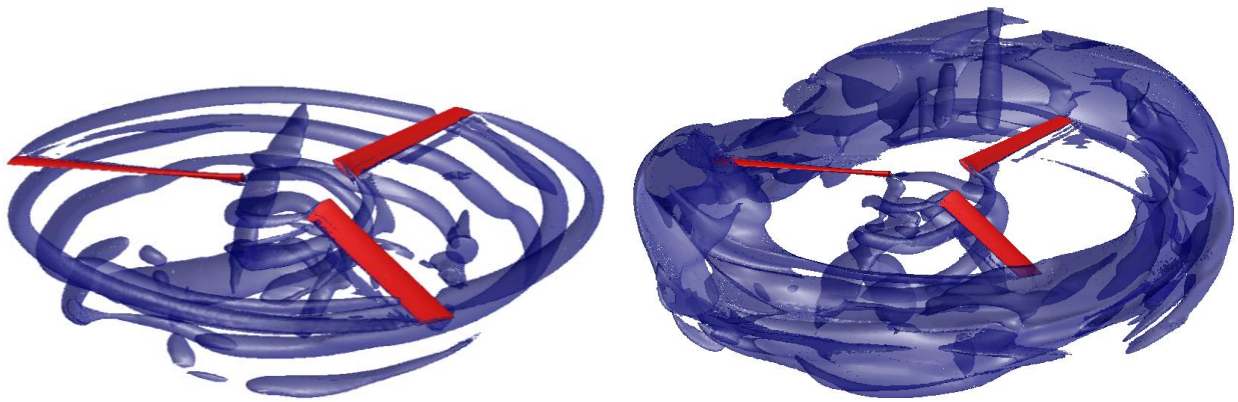


Figure 50: Visualization of the rotor wake with case 1 at Vz = -6.6 m/s CT = 0.0078 (L) and case 2 at Vz = -13.2 m/s CT = 0.0018 (R)

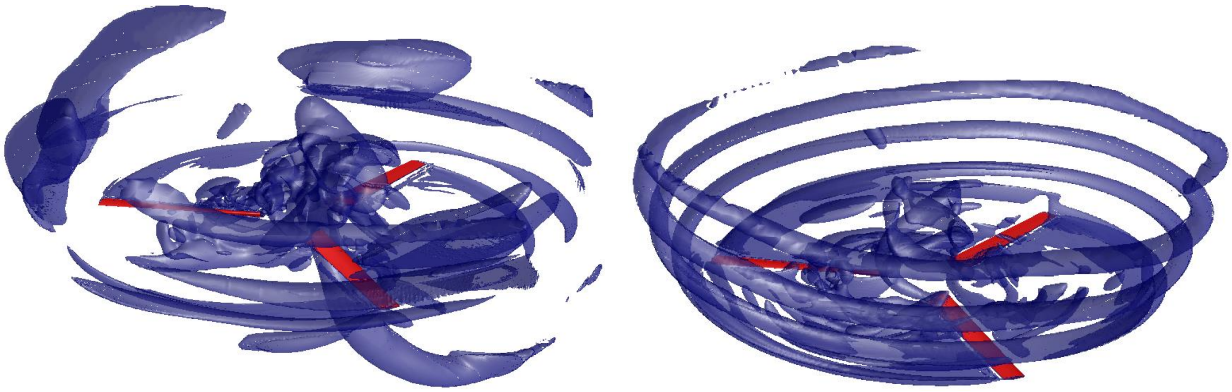


Figure 51: Visualization of the rotor wake with case 3 at Vz = -19.8m/s CT = 0.0045 (L) and case 4 at Vz = -26.4m/s CT = 0.0092

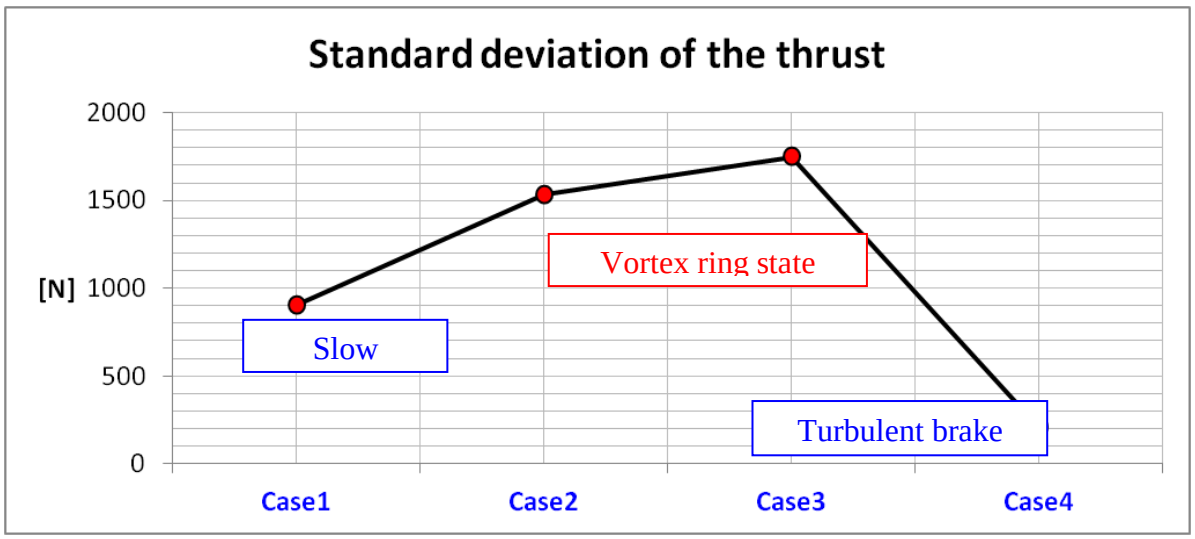


Figure 52: Thrust perturbations for the XV-15 isolated rotor descending into VRS

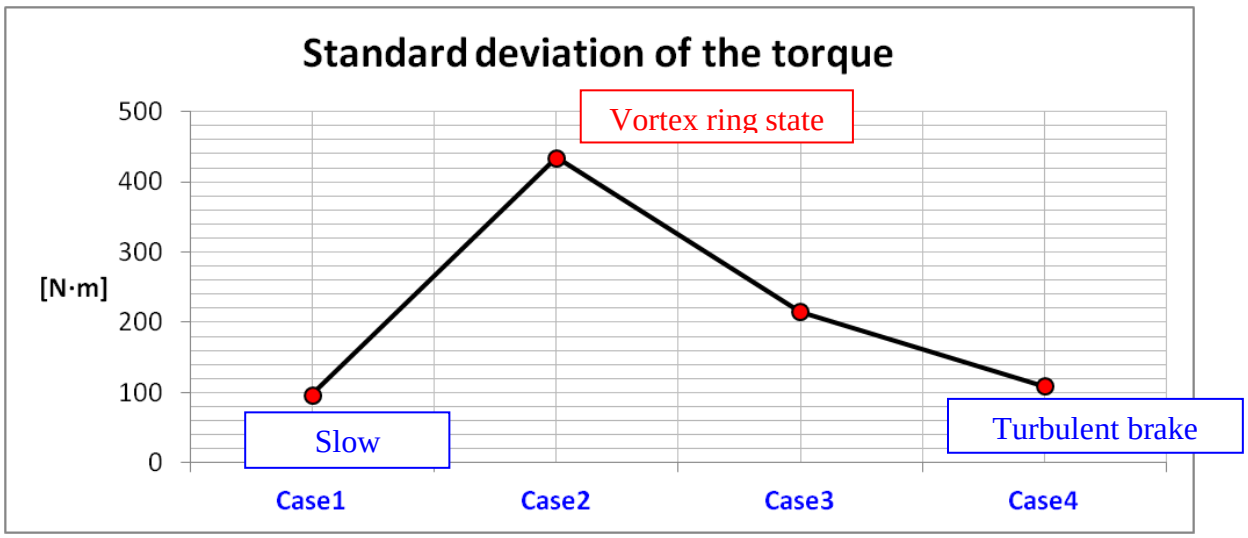


Figure 53: Torque perturbations for the XV-15 isolated rotor descending into VRS

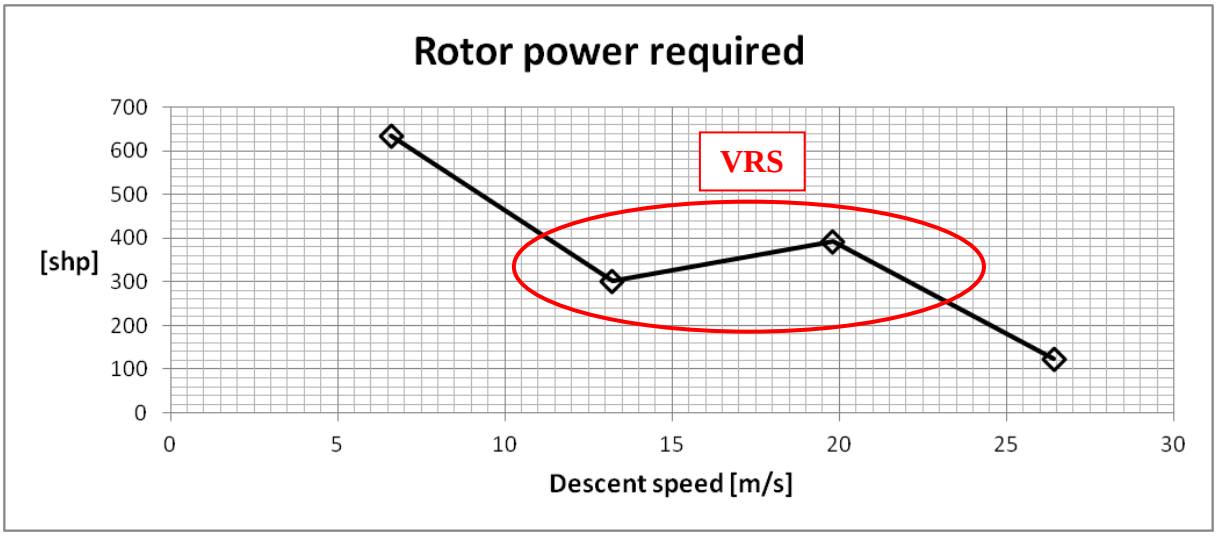


Figure 54: Measured total power in vertical descending flight through the vortex ring state

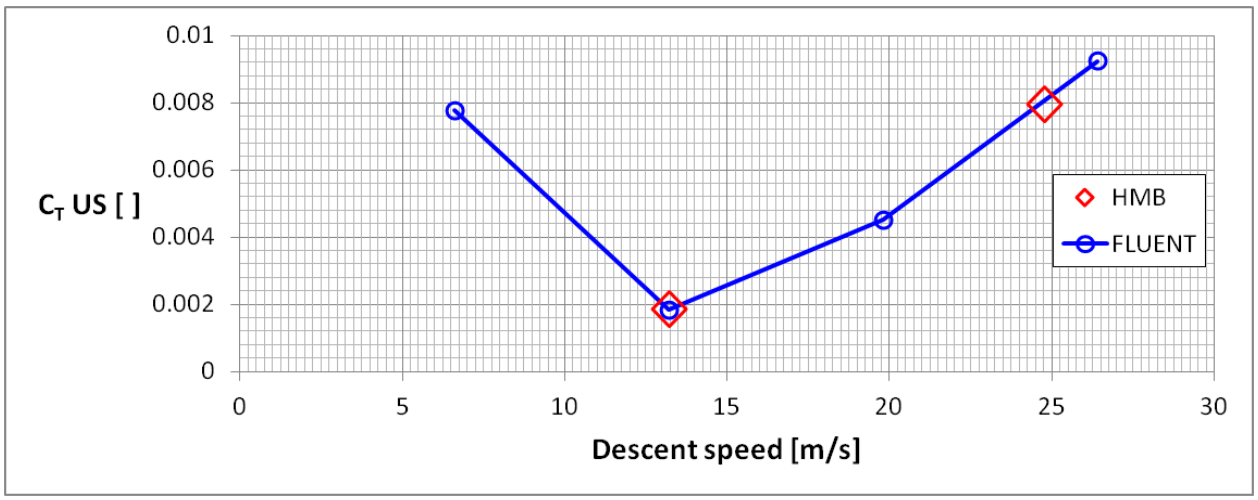


Figure 55: Predicted thrust coefficient, HMB vs FLUENT

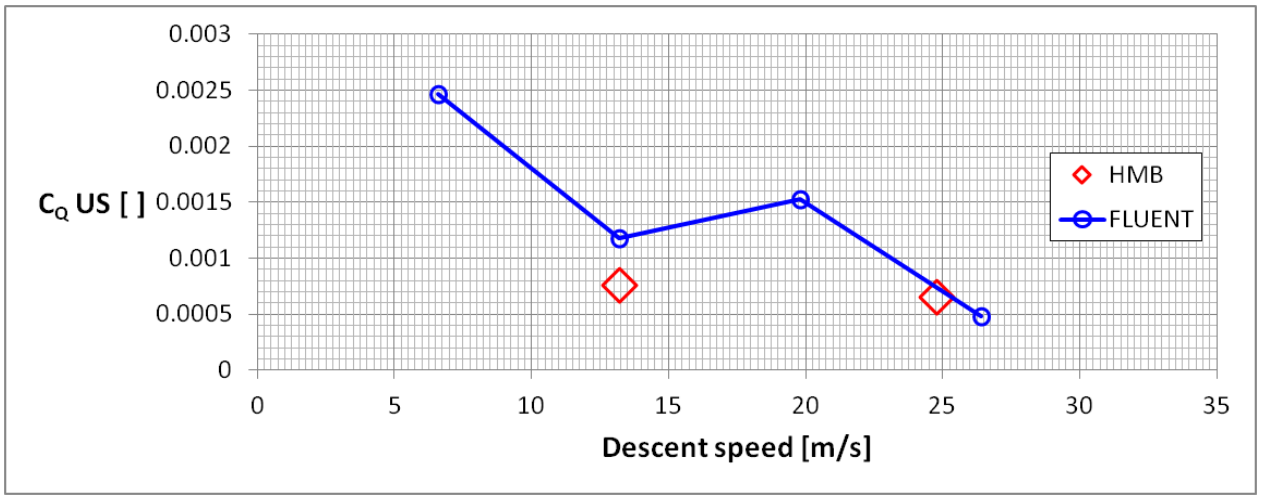


Figure 56: Predicted torque coefficient, HMB vs FLUENT